

1
2
3
4
5
6
7
8
9
10
11
12
13
14
15
16
17
18
19
20
21
22
23
24
25

Cross-Seasonal Impact of SST Anomalies over the Tropical Central Pacific Ocean on the Antarctic Stratosphere

Yucheng Zi^{1,2,3,4}, Zhenxia Long³, Jinyu Sheng², Gaopeng Lu⁴, Will Perrie^{2,3,5}, and Ziniu Xiao^{1,4}

Correspondence: Zhenxia Long (Zhenxia.Long@dfo-mpo.gc.ca) and Ziniu Xiao (xiaozn@lasg.iap.ac.cn)

¹ State Key Laboratory of Earth System Numerical Modeling and Application, Institute of Atmospheric Physics, Chinese Academy of Sciences, Beijing, China

² Department of Oceanography, Dalhousie University, Halifax, Nova Scotia, Canada

³ Fisheries and Oceans Canada, Bedford Institute of Oceanography, Dartmouth, Nova Scotia, Canada

⁴ School of Earth and Space Sciences, University of Science and Technology of China, Hefei, China

⁵ Department of Engineering Mathematics & Internetworking, Dalhousie University, Halifax, Canada

7 January 2026

26 **Abstract**

27 In this study we examine the cross–seasonal effects of boreal winter sea surface temperature
28 (SST) anomalies over the tropical central Pacific (Niño 4 region) on Antarctic stratospheric
29 circulation and ozone transport during the subsequent austral winter using ERA5 reanalysis of 45
30 years (1980–2024). Our analyses show that warm (cold) SST anomalies in the Niño 4 region
31 during December–February are associated with mid– and high–latitude stratospheric warming
32 (cooling), a contracted (expanded) stratospheric polar vortex (SPV), and enhanced (suppressed)
33 polar ozone concentrations in the subsequent July–September period. This delayed response is
34 mediated by the Pacific–South America (PSA) teleconnection pattern, which excites planetary
35 waves that propagate upward into the stratosphere, thereby modifying the Brewer–Dobson
36 circulation. In addition, as the influence of the Niño 4 SST anomalies on the PSA teleconnection
37 pattern diminishes during July–September, surface heat feedback at mid– and high–latitude
38 becomes critically important for planetary waves. For example, persistent southeastern Pacific
39 SST warming and sea-ice loss over the Amundsen and Ross Seas reinforce planetary waves by
40 releasing heat from ocean into atmosphere. A multivariate regression statistical model using
41 factors of boreal winter Niño 4 SST and June PSA indices explains approximately 32 % of the
42 variance in austral winter stratospheric temperatures. These findings highlight a previously
43 underexplored pathway through which tropical Pacific SST anomalies modulate Antarctic
44 stratospheric dynamics on seasonal timescales.

45

46 **Keywords:** Tropical central Pacific; Sea surface temperature; Antarctic Stratospheric warming;
47 stratospheric polar vortex (SPV); Pacific–South America (PSA) teleconnection; Antarctic sea-ice

48

49 **1 Introduction**

50 The Antarctic stratospheric circulation is largely governed by the wintertime Stratospheric
51 Polar Vortex (SPV), which is a major driver of weather and climate variability across the
52 Southern Hemisphere (Baldwin et al., 2021). Compared to its Northern Hemisphere counterpart,
53 the Antarctic SPV is generally more stable, owing to weaker thermal contrasts between the ocean
54 and land. Despite this stability, the Antarctic SPV exhibits considerable interannual variability
55 (Domeisen et al., 2019; Baldwin et al., 2021). Therefore, the Antarctic stratosphere plays a crucial
56 role in modulating weather and climate in the Southern Hemisphere through the seasonal
57 evolution of SPV and its dynamics processes and interaction with ozone chemistry (Thompson et
58 al., 2005; Solomon et al., 2016).

59 Previous studies revealed large interannual variations and long-term trends in the SPV,
60 stratospheric temperatures, and ozone concentrations (Karpetchko et al., 2005; Hu et al., 2022).
61 Superimposed on the long-term trends of SPV are substantial interannual variations and extreme
62 events (Shen et al., 2020; Zi et al., 2025; Lim et al., 2026). For instance, exceptionally weak SPV
63 episodes triggered by sudden stratospheric warmings (SSWs) occurred respectively in 2002, 2010,
64 2019, and 2024 (Thompson and Solomon, 2002; Esler et al., 2006; Laat and Weele 2011; Shen et
65 al., 2020; Zi et al., 2025; Lim et al., 2026), and an unusually strong SPV event driven by the
66 pronounced ozone depletion occurred in 2020 (Lim et al., 2024).

67 Several natural factors contribute to the above-mentioned SPV variability. The phase of the
68 Quasi-Biennial Oscillation (QBO), for instance, modulates planetary wave propagation and can
69 either strengthen or weaken the SPV (Kuroda et al., 2007). El Niño-Southern Oscillation (ENSO)
70 events also leave distinct warm- and cold-year signatures on Antarctic stratospheric temperatures
71 through changes in tropospheric wave forcing and the Brewer-Dobson (B-D) circulation (Yang
72 et al., 2015; Stone et al., 2022; Rao et al., 2023; Wang et al., 2025). Previous studies also suggest
73 sea-ice can have significant impact on the SPV (e.g., Rea et al., 2024; Song et al., 2025; Sun et al.,
74 2015), with implications for Southern Hemisphere climate variability. In addition, solar-cycle
75 variability contributes to interannual modulation by altering ultraviolet irradiance and
76 stratospheric heating rates (Kuroda et al., 2007). Alongside these natural drivers, fluctuations in
77 the atmospheric burdens of ozone-depleting substances and greenhouse gases continue to
78 influence both the magnitude and nature of Antarctic stratospheric variability (Singh and

79 Bhargawa, 2019).

80 ENSO is the most prominent mode of interannual climate variability (Wang, 2018).
81 Developing in boreal autumn and peaking in winter, ENSO influences the global weather patterns
82 through atmospheric teleconnections (McPhaden et al., 2006). It also modulates the SPV
83 primarily via the Pacific–North America (PNA) and the Pacific–South America (PSA) wave
84 trains (Garfinkel and Hartmann, 2008; Ineson and Scaife, 2009; Barriopedro and Calvo, 2014;
85 Polvani et al., 2017; Song and Son, 2018; Zhang et al., 2022). In the Northern Hemisphere, El
86 Niño events enhance tropical convection and amplify the PNA pattern, strengthening the Aleutian
87 Low, which in turn increases upward wave activity and weakens the SPV (Garfinkel and
88 Hartmann, 2008; Butler and Polvani, 2011; Zhang et al., 2022). In the Southern Hemisphere,
89 central Pacific (CP–type) El Niño events during September–February enhance convection near
90 the South Pacific Convergence Zone (SPCZ), which triggers the PSA wave trains that can
91 weaken the Antarctic SPV, resulting in stratospheric warming and ozone enhancement (Hurwitz
92 et al., 2011a,b; Yang et al., 2015; Manatsa and Mukwada, 2017; Domeisen et al., 2019; Ma et al.,
93 2022). In contrast, Eastern Pacific (EP–type) El Niño events were found to produce weaker
94 Antarctic stratospheric responses (Hurwitz et al., 2011a; Zubiaurre and Calvo, 2012).

95 Although many studies have examined the Antarctic stratosphere’s simultaneous or 1–2
96 months lag responses to ENSO from September to February (L’Heureux and Thompson, 2006;
97 Silvestri and Vera, 2009; Hu and Fu, 2010; Fogt et al., 2011; Lin et al., 2012; Kim et al., 2017;
98 Ma et al., 2022), our knowledge remains very limited on the ENSO’s cross–seasonal and delayed
99 effects (Manatsa and Mukwada, 2017; Niu et al., 2023). Some previous studies found that
100 delayed ozone responses occur in the year following an ENSO event (Lin and Qian, 2019), while
101 others suggested that tropical sea surface temperature (SST) anomalies as early as June can
102 influence stratospheric circulation later in the year (Grassi et al., 2008; Evtushevsky et al., 2015;
103 Lim et al., 2018; Stone et al., 2022). Yang et al. (2015) examined correlations between ENSO and
104 Antarctic stratospheric temperatures during July–September, but these were primarily interpreted
105 as concurrent responses. Despite these studies, the physical mechanisms by which ENSO events
106 in boreal winter influence the Antarctic stratosphere during the following austral winter
107 (July–September) remain poorly understood. During the austral winter, the SPV reaches its
108 maximum strength and also is particularly susceptible to dynamical disturbances. Consequently, a

109 deeper understanding of the delayed impacts of El Niño is crucial for improving prediction of
110 Antarctic stratospheric extreme events (Lin et al., 2009; Thompson et al., 2011).

111 The primary objective of this study is to examine how the boreal winter tropical central
112 Pacific SST anomalies (SSTa) influence the Antarctic stratosphere during the following austral
113 winter, with particular emphasis on the mechanisms through which tropical central Pacific SSTa
114 modulate Antarctic stratospheric dynamics, and associated planetary wave propagation and
115 mid-latitude sea-air interactions. The structure of this paper is as follows; Section 2 describes the
116 data and methodology; Section 3 presents quantification of the tropical central Pacific
117 SST-Antarctic stratosphere relationship; Section 4 shows an examination of the underlying
118 dynamical mechanisms; Section 5 presents the multivariate regression analysis; Section 6 shows
119 CMIP6 model validation; Section 7 is a summary and conclusion.

120

121 **2. Data and methods**

122 **2.1 Data**

123 The 6-hourly and monthly-mean atmospheric variables in the 45-year period 1980–2024
124 extracted from the ERA5 reanalysis (Hersbach et al., 2023a,b) are used in this study. This
125 reanalysis with a horizontal resolution of $1^{\circ} \times 1^{\circ}$ was generated by the European Centre for
126 Medium-Range Weather Forecasts (ECMWF). These atmospheric variables at 37 vertical
127 pressure levels include the geopotential height, horizontal and vertical winds, temperature, sea
128 level pressure (SLP), ozone mass mixing ratio, total column ozone (TCO₃), net surface downward
129 short-wave radiation flux, net surface upward long-wave radiation flux, latent and sensible heat
130 fluxes, outgoing long-wave radiation flux (OLR). The monthly sea surface temperature (SST) and
131 sea-ice concentration (SIC) during the same study period were also extracted from ERA5
132 reanalysis.

133 Several indices (such as Niño 3, Niño 3.4, and Niño 4) based on SST anomalies averaged
134 over a given region have been used to monitor the dynamic activities in the tropic Pacific
135 (Bamston et al. 1997; Trenberth, 1997). The Niño 3 index is the SST anomalies averaged over the
136 region between 5°N – 5°S and 150°W – 90°W , and has been used for monitoring and predicting
137 El Niño and La Niña events (Trenberth, 1997). The Niño 3.4 index is the SST anomalies
138 averaged over the region between 5°N – 5°S and 170°W – 120°W , and has been used as the

139 primary index for monitoring ENSO due to its ability to capture basin-scale variability (Bamston
 140 et al. 1997). The Niño 4 index is the SST anomalies averaged over the region between 5 °N–5 °S
 141 and 160 °E–150 °W, which is to monitor SST anomalies in the tropical central Pacific. In this
 142 study, the SST indices for the Niño 3, Niño 3.4, and Niño 4 were obtained from the HadISST1.1
 143 dataset (Rayner et al., 2003). Since results obtained after filtering the decadal component are
 144 similar, no filtering has been applied.

145 The Pacific–South America pattern (PSA) index was used to examine stratosphere and
 146 troposphere interactions, which was derived by projecting area–weighted SLP anomalies south of
 147 20 °S onto the second Empirical Orthogonal Function (EOF) mode (Mo and Higgins, 1998). All
 148 anomalies are calculated relative to the 1991–2020 daily and monthly climatology, and all data
 149 have been detrended. Statistical significance is assessed using the Student’s t-test.

150

151 **2.2 Method**

152 **2.2.1 Eliassen–Palm flux**

153 The Eliassen–Palm (E–P) flux is used to diagnose interactions between eddies and the
 154 zonal–mean flow in both the stratosphere and troposphere (Andrews et al., 1987). The E–P flux
 155 (\vec{F}) and its divergence ($\nabla \cdot \vec{F}$) are defined:

$$\vec{F} = (\vec{F}_\varphi, \vec{F}_p) = r_0 \cos \varphi \left\{ - [u'v'], \frac{f}{[\theta_p]} [v'\theta'] \right\} \quad (1)$$

$$\nabla \cdot \vec{F} = \frac{1}{r_0 \cos \varphi} \frac{\partial}{\partial \varphi} (\vec{F}_\varphi \cos \varphi) + \frac{\partial}{\partial p} (\vec{F}_p) \quad (2)$$

156 where u and v are the zonal and meridional wind components, respectively, and θ is the
 157 potential temperature. φ and p denote latitude and pressure, respectively. f is the Coriolis
 158 parameter, and r_0 is Earth’s radius. Square brackets [] indicate zonal averages, and primes (')
 159 denote deviations from the zonal mean.

160

161 **2.2.2 Takaya–Nakamura wave activity flux**

162 The Takaya–Nakamura (2001) wave activity flux (TN01 flux) has been used for determining
 163 the horizontal propagation of quasi-stationary Rossby waves in a zonally varying background
 164 flow (Takaya and Nakamura, 2001). The zonal (F_x) and meridional (F_y) components of TN01 are

165 defined as:

$$F_x = \frac{p}{2|U^\times|r_0^2} \left(\frac{U}{\cos \varphi} \left(\left(\frac{\partial \psi'}{\partial \lambda} \right)^2 - \psi' \frac{\partial^2 \psi'}{\partial \lambda^2} \right) + V \left(\frac{\partial \psi'}{\partial \lambda} \frac{\partial \psi'}{\partial \varphi} - \psi' \frac{\partial^2 \psi'}{\partial \lambda \partial \varphi} \right) \right) \quad (3)$$

$$F_y = \frac{p}{2|U^\times|r_0^2} \left(U \left(\frac{\partial \psi'}{\partial \lambda} \frac{\partial \psi'}{\partial \varphi} - \psi' \frac{\partial^2 \psi'}{\partial \lambda \partial \varphi} \right) + V \cos \varphi \left(\left(\frac{\partial \psi'}{\partial \varphi} \right)^2 - \psi' \frac{\partial^2 \psi'}{\partial \varphi^2} \right) \right) \quad (4)$$

166 where ψ represents the stream function, λ and φ denote longitude and latitude,
 167 respectively, and $|U^\times|$ is the magnitude of the total horizontal wind velocity. U and V are the
 168 climatological mean zonal and meridional wind components, respectively, while p is pressure,
 169 and r_0 is Earth's radius.

170

171 2.2.3 Residual mean meridional circulation

172 The Transformed Eulerian–Mean (TEM) formulation suggested by Andrews and McIntyre
 173 (1976, 1978) has widely been employed for diagnosing the large–scale circulation in the middle
 174 atmosphere. Different from the conventional Eulerian mean, the TEM framework accounts for
 175 eddy heat and momentum fluxes, thereby providing a more accurate representation of actual mass
 176 transport. In particular, the residual mean meridional circulation encapsulates the net effect of
 177 both mean flow and wave–induced eddy motions, making it especially useful for diagnosing
 178 stratospheric processes, such as B–D circulation and wave–driven anomalies associated with
 179 stratospheric warming. It is defined as:

$$[v]^* = [v] - \frac{1}{\rho_0} \frac{\partial}{\partial z} \left(\frac{\rho_0 [v'\theta']}{[\theta_z]} \right) \quad (5)$$

$$[w]^* = [w] - \frac{1}{r_0 \cos \varphi} \frac{\partial}{\partial \varphi} \left(\frac{\cos \varphi [v'\theta']}{[\theta_z]} \right) \quad (6)$$

180 where $[v]^*$ and $[w]^*$ denote the meridional and vertical components of the residual
 181 velocity, respectively. The vertical coordinate z is the log–pressure height defined as $z = -$
 182 $H \log \frac{p}{1000 \text{ hPa}}$, where H is the scale height (≈ 7 km). All other variables are consistent with those
 183 defined in Equations (1)–(4).

184

185 2.2.4 Quasi-geostrophic wave refraction index

186 The quasi-geostrophic wave refraction index (n^2) is also employed to diagnose the
 187 propagation characteristics of planetary waves (O'Neill and Youngblut, 1982). In general,
 188 planetary waves tend to propagate toward regions with a larger value of the refraction index. The
 189 formula is given as follows:

$$n^2 = \left[\frac{\bar{q}_\varphi}{r_0(\bar{u} - c)} - \left(\frac{k}{r_0 \cos \varphi} \right)^2 - \left(\frac{f}{2NH} \right)^2 \right] r_0^2 \quad (7)$$

190 where the meridional gradient of the zonal mean potential vorticity \bar{q}_φ is (Albers and
 191 Birner, 2014):

$$\bar{q}_\varphi = 2\Omega \cos \varphi - \left[\frac{(\bar{u} \cos \varphi)_\varphi}{r_0 \cos \varphi} \right] + \frac{r_0 f^2}{R_d} \left(\frac{p\theta \bar{u}_p}{T \bar{\theta}_p} \right)_p \quad (8)$$

192 Where u is the zonal-mean zonal wind; N, H, k, f, φ, r_0 and Ω are the buoyancy
 193 frequency, scale height, zonal wave number, the Coriolis parameter, latitude, Earth's radius and
 194 angular frequency of Earth, respectively. The subscripts refer to derivatives with respect to the
 195 given variable and the prime denotes the departure from the zonal mean.

196

197 2.2.5 CMIP6 datasets

198 To validate the observational results with model simulations, output from Phase 6 of the
 199 Coupled Model Intercomparison Project (CMIP6) are examined. Historical simulations were
 200 performed using fully coupled sea–air models forced with observed external drivers, including
 201 greenhouse gases, aerosols, volcanic eruptions, and solar variability. The analysis focuses on
 202 monthly mean SST, SIC, and temperature at 10 hPa over the period 1950–2014. A total of 24
 203 fully coupled CMIP6 models are included: CESM2, CESM2-FV2, CESM2-WACCM,
 204 CESM2-WACCM-FV2, E3SM-1-0, E3SM-1-1, E3SM-2-0, E3SM-2-1, CanESM5, CanESM5-1,
 205 HadGEM3-GC31-LL, HadGEM3-GC31-MM, CNRM-CM6-1, CNRM-ESM2-1, EC-Earth3-Veg,
 206 EC-Earth3-AerChem, ACCESS-CM2, BCC-CSM2-MR, CAS-ESM2-0, FIO-ESM-2-0,
 207 IPSL-CM6A-LR, NESM3, MRI-ESM2-0, MPI-ESM-1-2-HAM. Because these selected CMIP6
 208 models differ in their horizontal resolutions, to ensure consistency across datasets, all fields are
 209 interpolated onto a uniform $1^\circ \times 1^\circ$ latitude–longitude grid to ensure consistency across datasets.

210

211 **3 Impacts of SST anomalies on stratospheric atmospheric circulation**

212 To quantify the cross-seasonal response of the Antarctic stratospheric circulation to tropical
 213 Pacific SST anomalies, we first correlate three ENSO indices: Niño 4, Niño 3.4, and Niño 3, with
 214 the stratospheric temperature (T_{10-30}) and zonal wind (U_{10-30}) over Antarctica during the
 215 subsequent July–September period. Here, T_{10-30} refers to the zonal-mean temperature averaged
 216 over 60 °S–90 °S at 10–30 hPa, and U_{10-30} refers to the zonal-mean zonal wind averaged over
 217 40 °S–50 °S at the same pressure levels (Table 1).

218

219 **Table 1.** Correlation coefficients between the Niño 4, Niño 3.4 and Niño 3 indices and zonal-mean temperature
 220 index (T_{10-30}) averaged over 60 °S to 90 °S as well as zonal wind index (U_{10-30}) averaged over 40 °S to 50 °S at
 221 10–30 hPa.

	T_{10-30_Jul}	T_{10-30_Aug}	T_{10-30_Sep}	U_{10-30_Jul}	U_{10-30_Aug}	U_{10-30_Sep}
Niño 4_Sep	0.37***	0.36**	0.32**	-0.26*	-0.31**	-0.30**
Niño 4_Oct	0.35**	0.36**	0.34**	-0.22	-0.29*	-0.32**
Niño 4_Nov	0.37***	0.40***	0.32**	-0.22	-0.32**	-0.31**
Niño 4_Dec	0.38***	0.42***	0.35**	-0.24	-0.37***	-0.34**
Niño 4_Jan	0.42***	0.43***	0.30**	-0.31**	-0.40***	-0.33**
Niño 4_Feb	0.41***	0.41***	0.31**	-0.30**	-0.38***	-0.32**
Niño 4_Mar	0.38***	0.39***	0.30**	-0.23	-0.34**	-0.28*
Niño 3.4_Sep	0.34**	0.26*	0.20	-0.20	-0.21	-0.20
Niño 3.4_Oct	0.32**	0.27*	0.24	-0.19	-0.21	-0.23
Niño 3.4_Nov	0.34**	0.29*	0.23	-0.20	-0.23	-0.23
Niño 3.4_Dec	0.37***	0.31**	0.25*	-0.19	-0.24	-0.23
Niño 3.4_Jan	0.38***	0.32**	0.21	-0.24	-0.26*	-0.21
Niño 3.4_Feb	0.38***	0.32**	0.21	-0.25*	-0.26*	-0.21
Niño 3.4_Mar	0.36**	0.35**	0.25*	-0.23	-0.28*	-0.23
Niño 3_Sep	0.33**	0.22	0.14	-0.18	-0.17	-0.16
Niño 3_Oct	0.31**	0.21	0.18	-0.17	-0.16	-0.18
Niño 3_Nov	0.32**	0.23	0.19	-0.17	-0.18	-0.18
Niño 3_Dec	0.35**	0.25*	0.21	-0.16	-0.18	-0.18
Niño 3_Jan	0.35**	0.25*	0.16	-0.20	-0.19	-0.16
Niño 3_Feb	0.36**	0.27*	0.16	-0.20	-0.19	-0.15
Niño 3_Mar	0.29*	0.31**	0.20	-0.21	-0.23	-0.19

222

223 Note: Colors and asterisks denote statistical significance: red with *** for the 99 % confidence level,
 224 green with ** for 95 %, and magenta with * for 90 %.

225

226 Among the three indices, the Niño 4 index has the largest correlation with Antarctic
 227 stratospheric circulations (Table 1). In particular, the Niño 4 index exhibits a significantly
 228 positive correlation ($R \geq 0.30$, $p < 0.05$) with the subsequent July–September T_{10-30} index, with
 229 correlations from September to March reaching the 95 % confidence level. Here, the largest
 230 correlation occurs during the boreal winter (December–February), where the January Niño 4
 231 index shows the highest correlation with August T_{10-30} ($R = 0.43$, $p < 0.01$). Additionally, the
 232 December–February Niño 4 index is significantly negatively correlated with the July–September
 233 U_{10-30} index, with the largest negative correlation found between the January Niño 4 and August
 234 U_{10-30} ($R = -0.40$, $p < 0.01$). These correlations are consistent with stratospheric warming (cooling)
 235 and a weakened (strong) Stratospheric polar vortex (SPV) associated with warm (cold) SSTa in
 236 the tropical central Pacific.

237 In comparison with the Niño 4, the Niño 3.4 index has weaker correlations with
 238 stratospheric temperature and zonal wind. The January and February Niño 3.4 have the highest
 239 correlation with July T_{10-30} ($R = 0.38$, $p < 0.01$), while the correlation with September T_{10-30} is not
 240 statistically significant. Similarly, its correlation with U_{10-30} is weak, with only a marginally
 241 significant negative correlation between the January–March Niño 3.4 index and August U_{10-30} at
 242 the 90 % confidence level. However, the Niño 3 index exhibits the weakest correlation with the
 243 polar stratospheric temperature and zonal wind. While a moderate correlation with T_{10-30} is
 244 observed during July–August, correlations in September are very weak and do not exceed the
 245 90 % significance threshold.

246 We next examine the connection of ENSO phases in the preceding boreal winter with the
 247 Antarctic stratospheric circulation anomalies in July–September for 45 years 1980–2024 (Table
 248 2). Here, we define a warm (cold) stratospheric year as the year when the July–September mean
 249 T_{10-30} index is ≥ 0.5 (≤ -0.5) standard deviations (σ) or when the U_{10-30} index is $\leq -0.5\sigma$ ($\geq 0.5\sigma$).
 250 During the study period of 45 years, 14 are boreal winter El Niño years, of which 8 are followed
 251 by stratospheric warming events and 4 by cooling events, corresponding to an occurrence rate of
 252 57 % and 28.5 %, respectively. Notably, 6 out of these 8 warming cases occur after central Pacific
 253 El Niño events. The remaining two cases, 2015/16 and 2023/24, are classified as eastern Pacific
 254 El Niño events, but are also accompanied by warm SSTa in the tropical central Pacific. By
 255 comparison, among 17 boreal winter La Niña years, 11 are followed by stratospheric cooling

256 events and 4 by warming events, corresponding to occurrence rates of 65 % and 23.5 %,
 257 respectively. Of the 13 ENSO-neutral years, four are associated with stratospheric warming
 258 events and another four with cooling events, indicating no clear preference for either condition
 259 during neutral years.

260

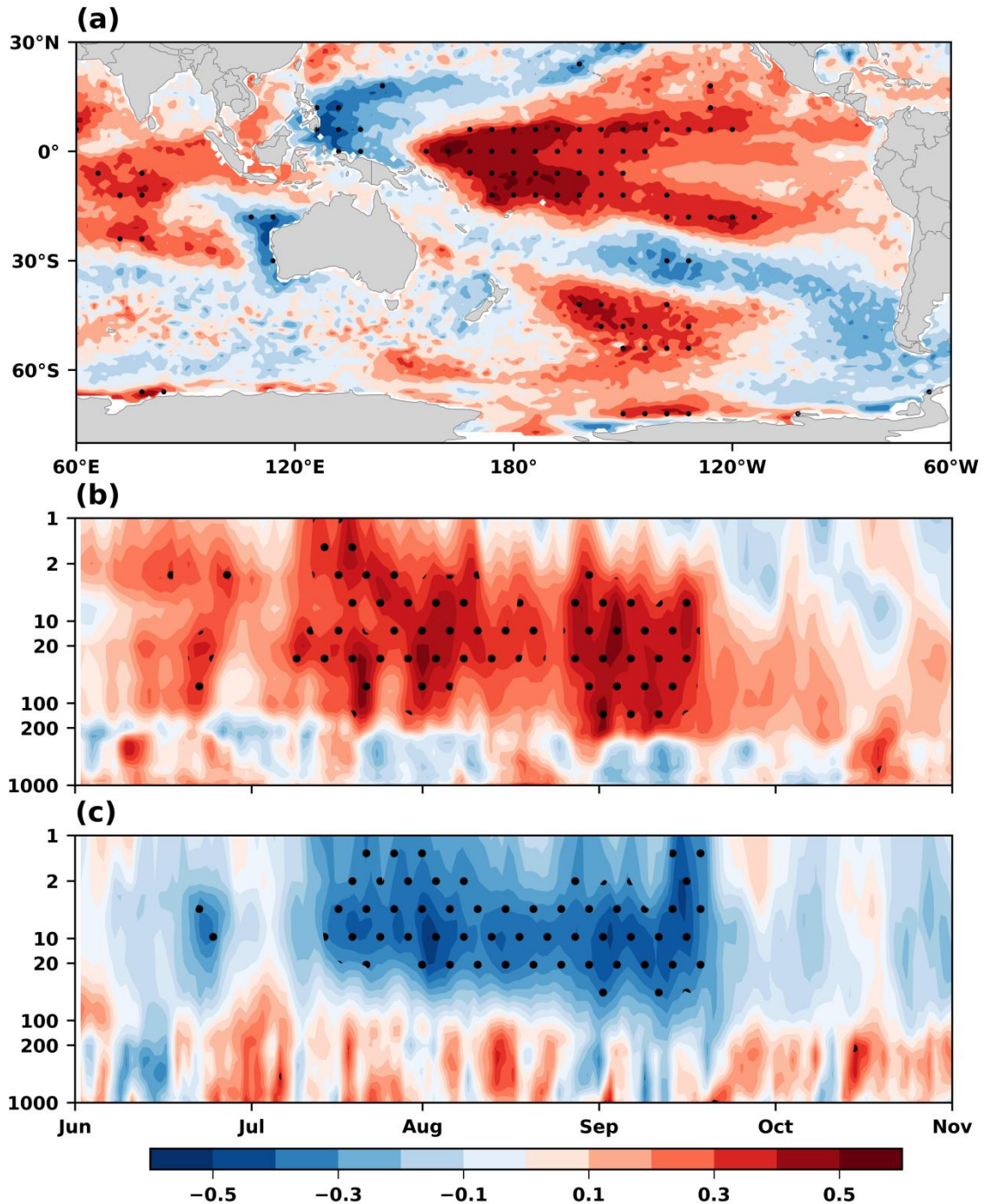
261 **Table 2.** Relationship between ENSO phases in the preceding boreal winter and Antarctic stratospheric
 262 temperature (AST) anomalies during July–September for the 45-year period (1980–2024).

Year (DJF)	Event Type	AST Anomalies	Year (DJF)	Event Type	AST Anomalies
1980–1981	Neutral	Cold (C)	2002–2003	El Niño (CP)	C
1981–1982	Neutral	C	2003–2004	Neutral	W
1982–1983	El Niño (EP)	C	2004–2005	El Niño (CP)	W
1983–1984	La Niña	Warm(W)	2005–2006	La Niña	C
1984–1985	La Niña	Normal (N)	2006–2007	El Niño (CP)	W
1985–1986	Neutral	W	2007–2008	La Niña	C
1986–1987	El Niño (CP)	C	2008–2009	La Niña	C
1987–1988	El Niño (CP)	W	2009–2010	El Niño (CP)	W
1988–1989	La Niña	C	2010–2011	La Niña	C
1989–1990	Neutral	N	2011–2012	La Niña	W
1990–1991	Neutral	C	2012–2013	Neutral	N
1991–1992	El Niño (CP)	W	2013–2014	Neutral	N
1992–1993	Neutral	N	2014–2015	El Niño (CP)	C
1993–1994	Neutral	N	2015–2016	El Niño (EP)	W
1994–1995	El Niño (CP)	N	2016–2017	La Niña	W
1995–1996	La Niña	W	2017–2018	La Niña	C
1996–1997	Neutral	W	2018–2019	El Niño (CP)	W
1997–1998	El Niño (EP)	C	2019–2020	Neutral	C
1998–1999	La Niña	C	2020–2021	La Niña	C
1999–2000	La Niña	C	2021–2022	La Niña	C
2000–2001	La Niña	C	2022–2023	La Niña	N
2001–2002	Neutral	W	2023–2024	El Niño (EP)	W
El Niño		La Niña		Neutral	
Total: 14		Total: 17		Total: 13	
Warm (CP) / Cold		Warm / Cold		Warm / Cold	
8 (6) / 4		4 / 11		4 / 4	
57% / 28.5%		23.5% / 65%		31% / 31%	

263

264 Correlation coefficients between the July–September mean T_{10-30} index and the global SST
 265 field from the preceding boreal winter are shown in Figure 1a. The highest correlation
 266 coefficients are observed in the central Pacific, particularly over the Niño 4 region. Additionally,

267 significant positive correlations appear over the North Indian Ocean and the South Pacific, likely
 268 reflecting remote responses to ENSO (Alexander et al., 2002).
 269



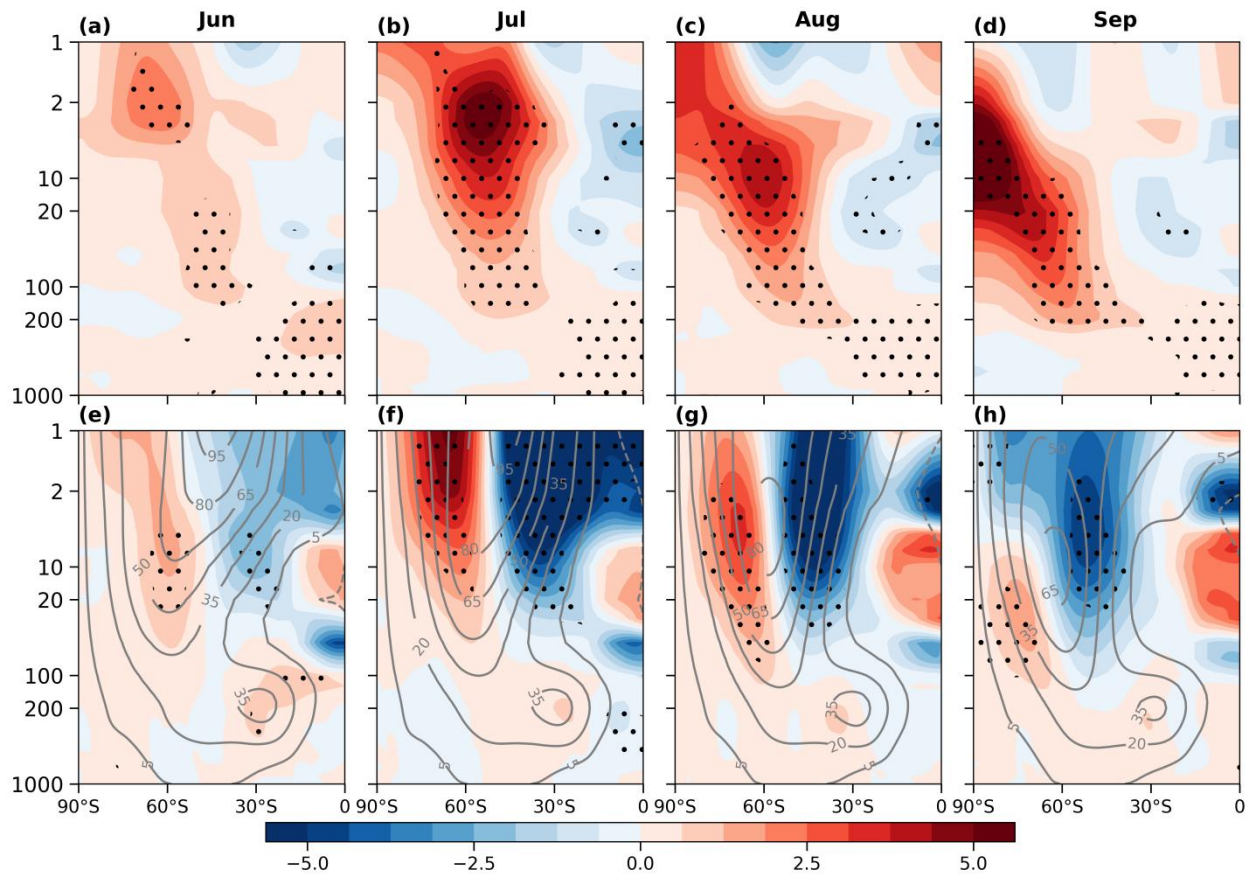
270
 271 **Figure 1.** (a) Correlation coefficients between July–September mean T_{10-30} index and January–March mean
 272 SST, (b) Correlation coefficients between December–February mean Niño 4 index and daily Temperature
 273 averaged over 60°S–90°S, and (c) same as (b), but for zonal-mean zonal wind averaged over 40°S–50°S.
 274 Black dots represent the 95% confidence level.

275 The most pronounced impacts of SSTa over the Niño 4 region occur, however, above 100

276 hPa during the austral winter of the following year. Figs. 1b-c present the correlations between
277 the boreal winter Niño 4 index and the Antarctic daily zonal-mean temperature (averaged over
278 60 °S–90 °S) and zonal-mean zonal wind (averaged over 40 °S–50 °S) from June to September of
279 the following year. The Niño 4 index exhibits significant positive correlations with stratospheric
280 temperature and negative correlations with zonal wind during July–September (Figs. 1b-c),
281 consistent with the stratospheric warming and weakened SPV.

282 To further examine the impacts of the Niño 4 SST anomalies on the stratospheric
283 temperatures and the SPV, 17 warm years and 14 cold years according to $\pm 0.5\sigma$ of the Niño 4
284 index are selected to calculate composite differences in vertical zonal-mean temperature and
285 zonal wind (Figs. 2). The $\pm 0.5\sigma$ of threshold value is chosen to capture relatively strong warm and
286 cold events, but the results are not sensitive to the specific threshold value. In June, warming is
287 primarily observed in the upper polar stratosphere and the tropical troposphere, with the strongest
288 signal at 1–5 hPa (Fig. 2a). As the season progresses, the warming intensifies and gradually
289 propagates downward and poleward, with peak anomalies centered around $\sim 50^\circ\text{S}$ in July–August
290 (Figs. 2b–c). This warming reaches its maximum at 10 hPa around 70°S – 90°S in September
291 (Figs. 2d).

292



293

294 **Figure 2.** Composite differences between warm and cold Niño 4 years for (a,e) June, (b,f) July, (c,g) August,
 295 and (d,h) September. (a–d) Zonal–mean temperature (shaded, unit: K), and (e–h) zonal–mean zonal winds
 296 (shaded, unit: m/s), where the climatological mean of zonal-mean zonal wind is computed from 1991–2020
 297 (contour, unit: m/s). Black dots indicate regions statistically significant at the 95% confidence level.

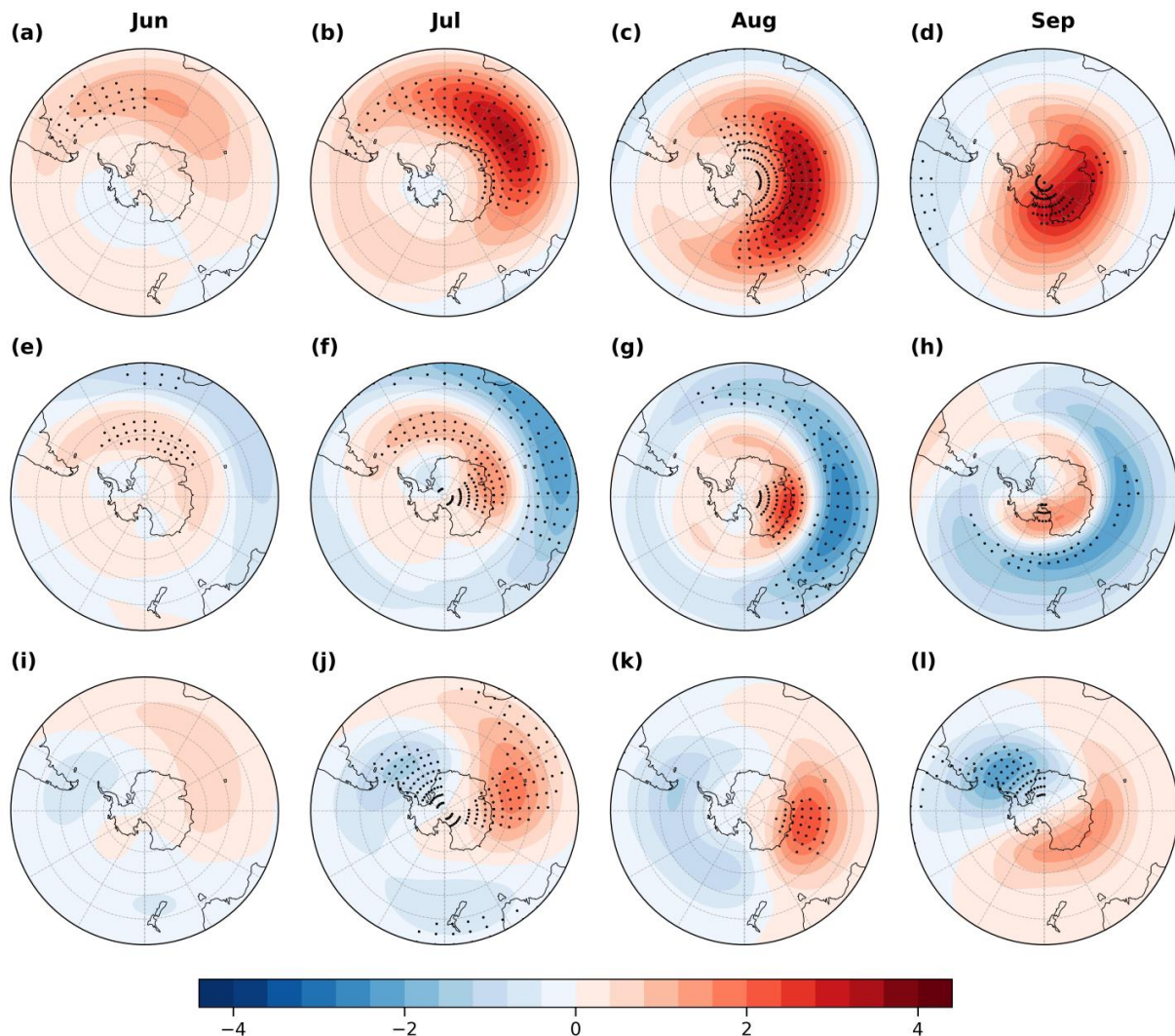
298

299 In general, the stratospheric warming anomalies are accompanied by a significant weakening
 300 of the stratospheric westerlies. Under climatological conditions, the polar night jet typically
 301 establishes and strengthens gradually from June to July, centered near 1 hPa and around 45 °S
 302 (Figs. 2e–f). The jet core then migrates poleward and downward in August and weakens in
 303 September (Figs. 2g–2h). However, during warm Niño 4 years, anomalous easterlies emerge
 304 north of 45 °S and anomalous westerlies develop south of 45 °S as early as June (Fig. 2e), while
 305 anomalous easterlies progressively shift poleward from July to September, substantially
 306 weakening the climatological westerlies (Figs. 2f–h), indicating a notable poleward contraction
 307 and shift of the SPV (Figs. 2f–h). This pattern reflects a delayed yet robust stratospheric response
 308 to warm SST anomalies in the tropical central Pacific.

309 Moreover, the atmospheric responses exhibit the maximum stratospheric warming appears
 310 over the Indian Ocean during June–September, while no significant warming is observed in the

311 South Pacific (Fig. 3a-d). This warming pattern tends to weaken mid-latitude baroclinicity,
 312 producing a westerly anomaly at high-latitude and an easterly anomaly in the mid-latitude in
 313 stratosphere, indicative of a contraction of the jet stream (Figs. 3e-h). Meanwhile, the
 314 stratospheric geopotential height show a zonal wave-1 pattern, with a positive center over the
 315 Indian Ocean and a negative center over the Pacific and Atlantic, suggesting a role of planetary
 316 wave (Figs. 3i-l). The responses intensify from June to September and gradually propagate
 317 eastward and poleward (Fig. 3). For example, the maximum westerly anomalies extend into the
 318 Pacific polar region by September, while pronounced easterly anomalies develop over the
 319 mid-latitude Pacific (Fig. 3h).

320



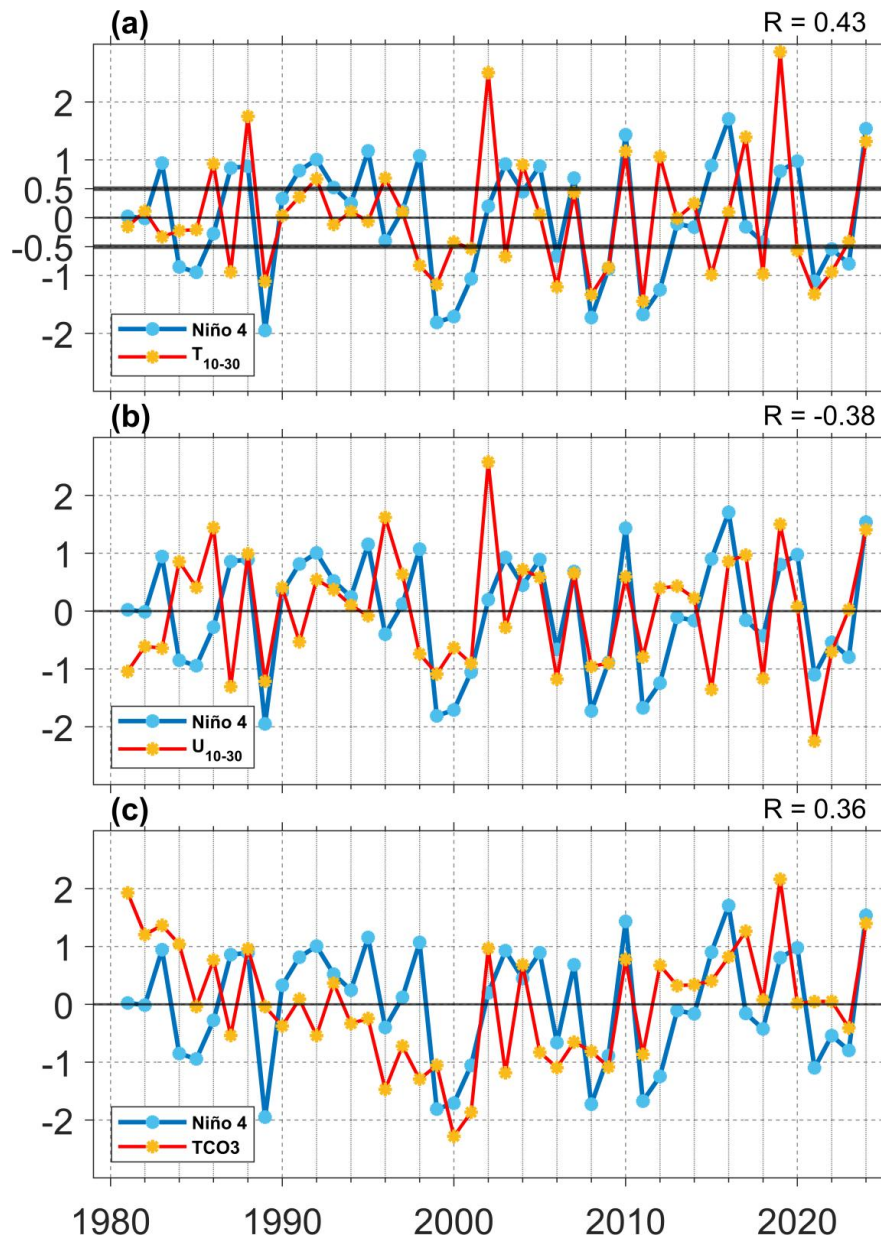
321

322 **Figure 3.** Composite differences between warm and cold Niño 4 years for (a,e,i) June, (b,f,j) July, (c,g,k)
 323 August, and (d,h,l) September. (a–d) Temperature averaged over 10–30 hPa (shaded, unit: 2 K), (e–h)
 324 zonal wind averaged over 10–30 hPa (shaded, unit: 5 m/s), and (i–l) geopotential height averaged over 10–30 hPa
 325 (shaded, unit: 10 dagpm). Black dots indicate regions statistically significant at the 95% confidence level.

326

327 Following previous studies (Rao et al., 2020; Baldwin et al., 2021; Zi et al., 2025; Lim et al.,
328 2026), the Antarctic stratospheric temperature index (T_{10-30}) is used to examine the stratospheric
329 response. Although the strongest and most statistically significant correlations between the
330 December–February Niño 4 index and the subsequent July–September Antarctic stratospheric
331 temperature are found over the region spanning approximately 30°E – 160°W and 55°S – 75°S
332 (Fig. 3b-d), the T_{10-30} index provides a robust and representative diagnostic of Antarctic
333 stratospheric warming, exhibiting a high correlation coefficient ($R = 0.93$) with the temperature
334 index averaged over 30°E – 160°W and 55°S – 75°S .

335 Figures 4a–b present time series of the boreal winter Niño 4 index alongside the
336 July–September mean T_{10-30} and U_{10-30} indices from 1981–2024. The Niño 4 index exhibits a
337 significant positive correlation with the T_{10-30} index ($R = 0.43$, $p < 0.01$) (Fig. 4a) and a
338 significant negative correlation with the U_{10-30} index ($R = -0.38$, $p < 0.01$) (Fig. 4b), both are
339 significant at the 99 % confidence level, indicating that a warm (cold) Niño 4 SSTa is typically
340 associated with a warmer (colder) polar stratosphere and contracted (expanded) SPV. Notably,
341 several prominent sudden stratospheric warming (SSW) events (e.g., 1988, 2019, 2024) coincide
342 with positive Niño 4 SSTa (Fig. 4a). The associated stratospheric changes also influence Antarctic
343 ozone concentrations (Wang et al., 2025). For instance, TCO_3 index also shows a strong positive
344 correlation with both the T_{10-30} index ($R = 0.56$, $p < 0.01$) and the boreal winter Niño 4 index ($R =$
345 0.36 , $p < 0.01$), both statistically significant at the 99 % confidence level (Fig. 4c). This suggests
346 that warm (cold) Niño 4 events enhance (suppress) poleward ozone transport, thereby increasing
347 (decreasing) ozone concentrations over Antarctica.



348

349

350

351

352

353

354 4 Effects of anomalous planetary waves

355 4.1 Stratospheric temperature and zonal wind

356

357

358

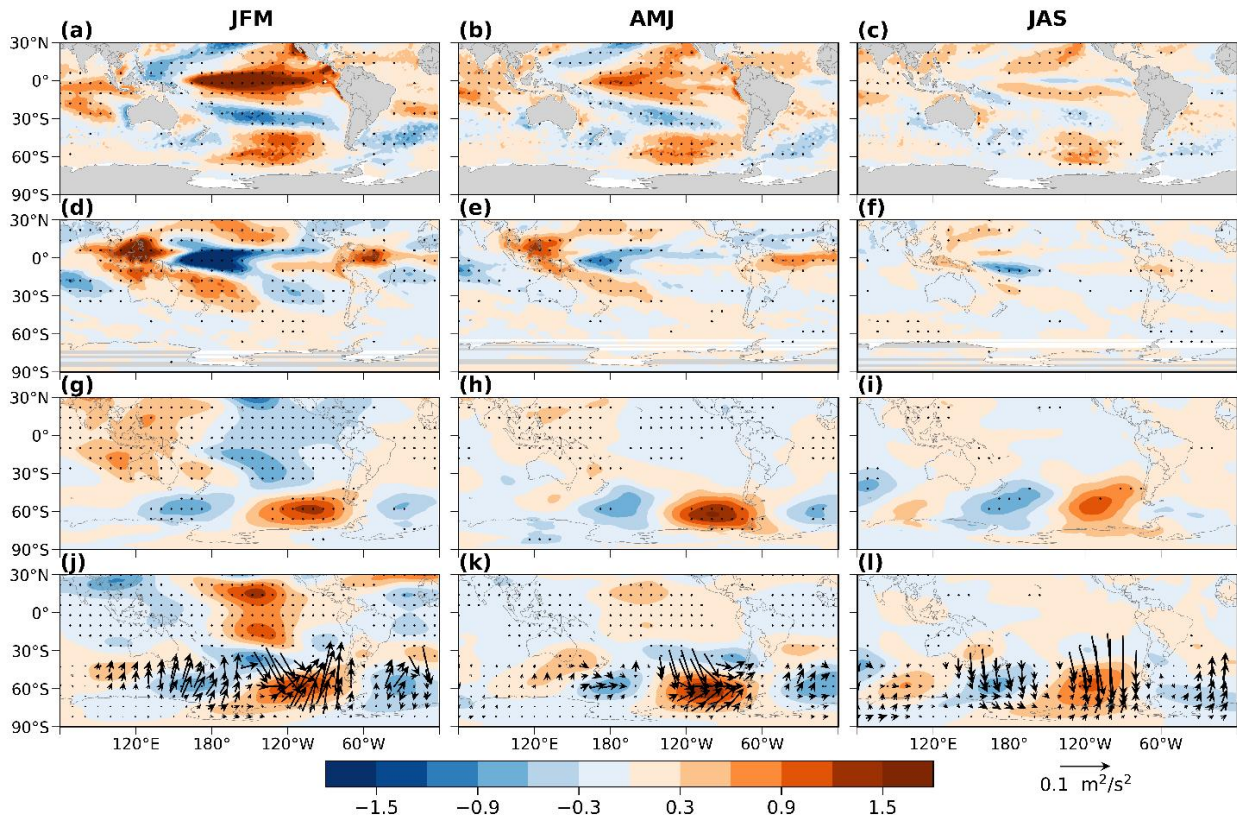
359

Figure 4. Time series of standardized Niño 4 index (blue line), along with (a) July–September mean T_{10-30} index (red line), (b) July–September mean U_{10-30} index (red line, multiplied by -1), and (c) July–September mean TCO_3 index (red line) from 1981 to 2024. R in the upper right corner denotes the correlation coefficient between the Niño 4 index and the T_{10-30} , U_{10-30} , and TCO_3 indices, respectively.

360 events, the composite differences of key atmospheric variables were calculated between warm
361 and cold Niño 4 years, averaged over consecutive three-month periods from January to
362 September of the following year.

363 During the mature phase of El Niño (January–March), positive SST anomalies develop in
364 the tropical central and eastern Pacific (Fig. 5a). As SST increases, convection intensifies in the
365 central Pacific (Fig. 5d), accompanied by a negative SLP anomaly and a positive geopotential
366 height anomaly at 250 hPa over the tropical central Pacific, indicating a barotropic response (Figs.
367 5g,j). Furthermore, the convection anomaly triggers a southward–propagating teleconnection
368 wave train at 250hPa, as suggested by the TN01 flux (Vector, Fig. 5j). This wave train, known as
369 the PSA teleconnection (Mo and Higgins, 1998), features a positive geopotential height anomaly
370 over the southeastern Pacific (near 110 °W, 60 °S) and a negative geopotential height anomaly
371 over the southwestern Pacific (near 150 °W, 40 °S) (Fig. 5j). The warm Niño 4 SSTa and their
372 associated convection responses over the tropical central Pacific persist into April–June (Figs.
373 5b,e,h,k). Although the amplitude of the positive and negative height centers over the
374 southeastern and southwestern Pacific weakens, the PSA wave train remains active (Fig. 5k). By
375 July–September (austral winter), however, the warm Niño 4 SSTa and their associated barotropic
376 responses begin to dissipate (Figs. 5c,i,l). Nevertheless, the negative and positive height center
377 are still persists in the southwestern and southeastern Pacific regions, respectively, as indicated by
378 the TN01 flux (Fig. 5l).

379



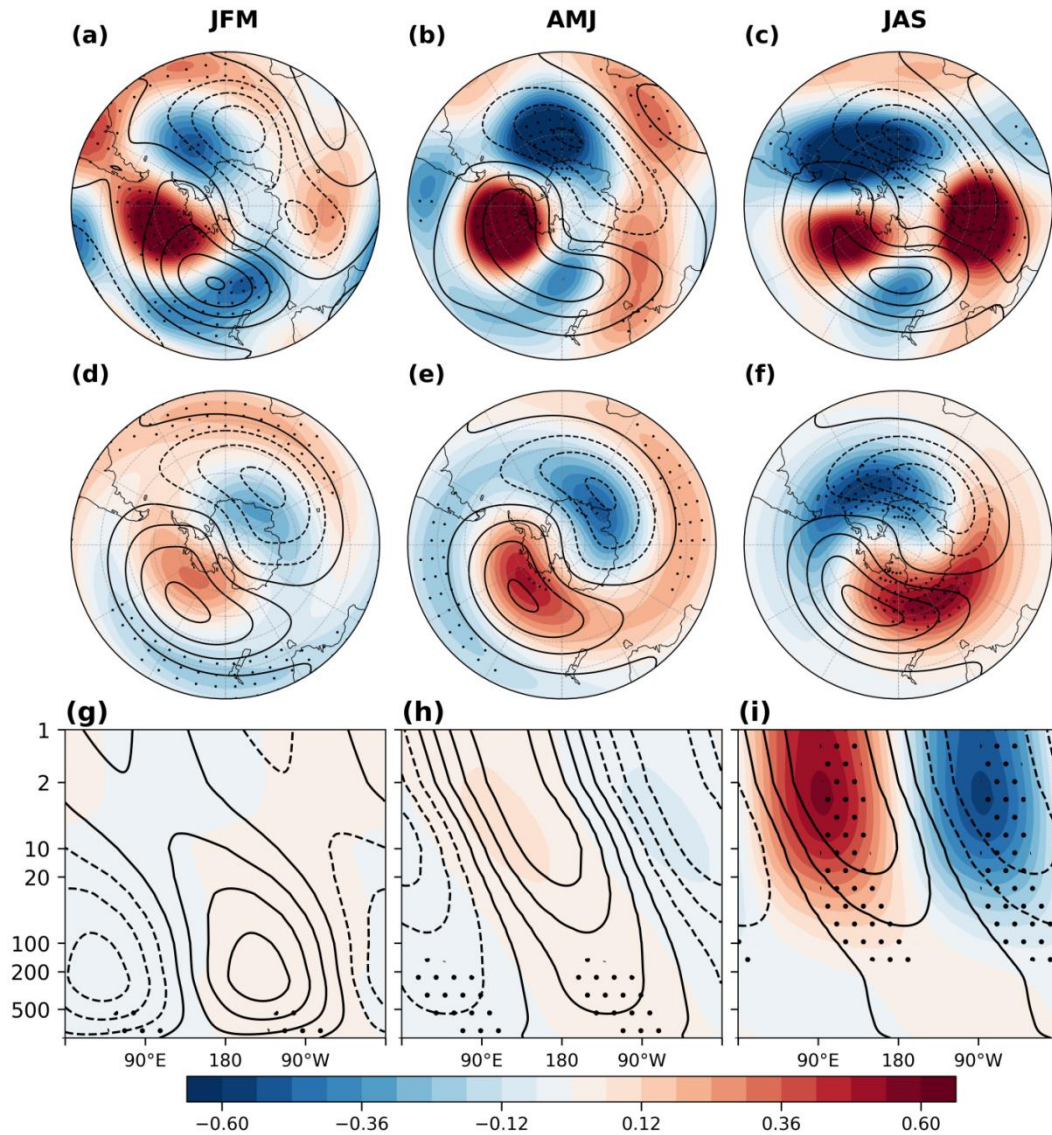
380
 381 **Figure 5.** Composite differences between warm and cold Niño 4 years. The panels show three-month means
 382 for January–March (left column), April–June (middle column), and July–September (right column). (a–c) Sea
 383 surface temperature (SST, shaded, unit: K), (d–f) outgoing longwave radiation (OLR, shaded, unit: 1.5×10^6
 384 W/m^2), (g–i) sea level pressure (SLP, shaded, unit: 300 Pa), (j–l) Geopotential heights (shaded, unit: 5 dagpm)
 385 and TN01 flux (vector, unit: $0.1 \text{ m}^2/\text{s}^2$) at 250 hPa. Black dots indicate regions statistically significant at the
 386 95% confidence level.

387

388 The geopotential height anomaly extends into the lower stratosphere and remains
 389 statistically significant at 100 hPa (Fig. 6a–f). The climatological geopotential height at 100 hPa is
 390 characterized by a wave-1 pattern, featuring a positive height center over the South Pacific and a
 391 negative height center over the South Atlantic Ocean and South Indian Ocean sectors (contour
 392 lines in Fig. 6a–f). During January–February–March (JFM) (austral summer), geopotential height
 393 anomalies associated with warm tropical central Pacific SSTa form a wave train, with two
 394 positive centers over the southeastern Indian Ocean and southeastern Pacific, and two negative
 395 centers over the southwestern Pacific and the southern Atlantic (Fig. 6a). However, this pattern at
 396 high-latitude are not statistically significant (Fig. 6d). Although the wave-1 component of the
 397 geopotential height shows a westward tilt with altitude and broadly resembles with the
 398 climatological structure, this alignment is only statistically significant below 500 hPa (Fig. 6g).
 399 As a result, planetary waves are not substantially amplified in the lower stratosphere, primarily

400 due to the prevailing easterly winds in the upper stratosphere over Antarctica in JFM (contours,
 401 Fig. 7a), which inhibit upward propagation of planetary waves (Baldwin et al., 2021). This is
 402 further supported by the E–P flux vectors, which show that planetary wave propagation is largely
 403 confined below 50 hPa in the mid- and low-latitudes (Fig. 7a).

404



405

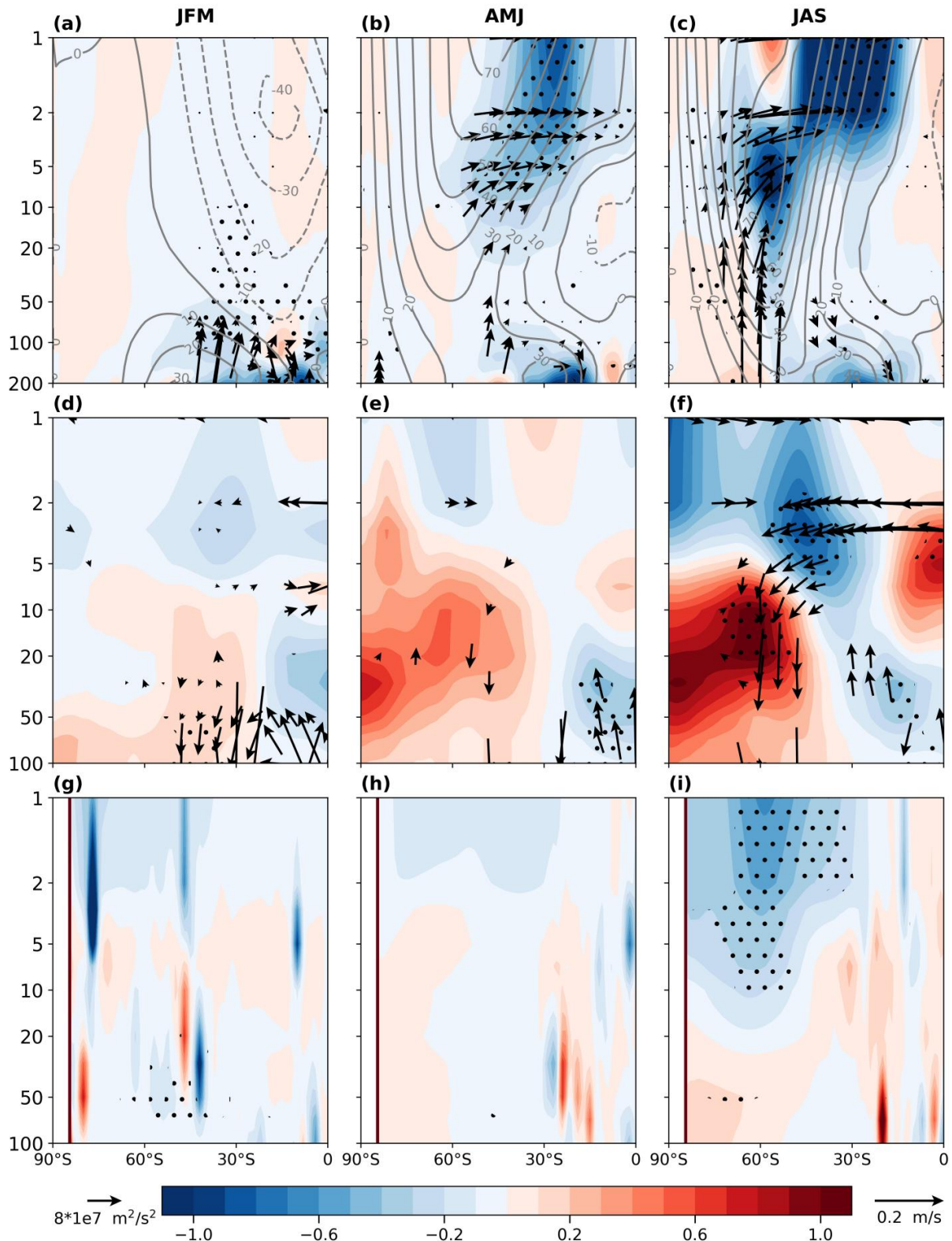
406 **Figure 6.** Composite differences between warm and cold Niño 4 years. The panels show three-month means
 407 for January–March (left column), April–June (middle column), and July–September (right column). (a–c)
 408 Geopotential heights at 100 hPa (shaded, unit: 5 dagpm), (d–f) wave-1 of geopotential heights at 100 hPa
 409 (shaded, unit: 5 dagpm), and (g–i) wave-1 of geopotential heights averaged over 45°S–75°S at 1000–1hPa
 410 (shaded, unit: 30 dagpm). The climatological geopotential height is calculated from 1991–2020 (contours, unit:
 411 dagpm). Black dots indicate regions statistically significant at the 95% confidence level.

412

413 During April-May-June (AMJ), the positive geopotential height center over the southeastern

414 Pacific and the negative center over the southern Atlantic become more pronounced (Fig. 6b),
415 aligning more closely with the climatological wave-1 pattern (Fig. 6e). This alignment
416 contributes to a westward tilt of the geopotential height field with altitude (Fig. 6h). However,
417 this vertical tilt is only statistically significant below 100 hPa (Fig. 6h). During this period,
418 stratospheric zonal winds gradually transition to a westerly regime, but large portions of the
419 upper polar stratosphere continue to experience weak westerlies or even easterlies (contours, Fig.
420 7b). As a result, a significant portion of the planetary waves are refracted equatorward, and their
421 ability to disturb the polar stratosphere remains limited (Fig. 7b).

422



423

424 **Figure 7.** Composite differences between warm and cold Niño 4 years. The panels show three-month means
 425 for January–March (left column), April–June (middle column), and July–September (right column). (a–c) E–P
 426 flux (vector: m^2/s^2) and its divergence (shaded, unit: 60 m/s/day), where the climatological zonal-mean zonal
 427 wind are calculated from 1991–2020 (contours, unit: m/s), (d–f) ozone mass mixing ratio (shaded, unit: 3×10^{-6}
 428 kg/kg) and residual mean circulation (vector, unit: m/s), and (g–i) wave reflective index (shaded, unit: %).
 429 Black dots indicate regions statistically significant at the 95% confidence level.

430 During July-August-September (JAS), the geopotential height centers over the southeastern
431 Pacific weaken, while the positive center over the southern Indian Ocean strengthens
432 significantly (Fig. 6c). This spatial pattern enhances the climatological wave-1 trough and ridge
433 structure (Fig. 6f) and exhibits a westward tilt of the geopotential height field with height, which
434 becomes statistically significant in the stratosphere (Fig. 6i). Although the wave-2 pattern exhibits
435 a strong amplitude, it is nearly orthogonal to the climatological wave-2 phase (Figures not
436 shown). Therefore, the wave-2 component is not reinforced, and the process is mainly dominated
437 by the wave-1 pattern. During this period, the polar regions enter the polar night, with minimal
438 solar heating, which increases baroclinicity in the mid- and high- latitude. The stratosphere
439 becomes fully dominated by westerly winds, creating favorable conditions for the upward
440 propagation of planetary waves into the polar stratosphere (contour lines, Fig. 7c). In addition, the
441 wave reflection index exhibits a significant negative anomaly south of 30 °S in the upper
442 stratosphere (Fig. 7i). This further indicates that planetary waves are strongly refracted toward the
443 mid- and high-latitude stratosphere (Fig. 7c). Based on the E-P flux theorem (Matsuno, 1971),
444 when E-P flux convergence occurs in the mid-latitudes, the jet stream tends to weaken and
445 poleward heat transport increases. During this stage, the strong SPV inhibits the poleward
446 propagation of planetary waves, resulting in relatively weak polar warming and stronger warming
447 in the subpolar and mid-latitude regions. As a result, significant mid- and high-latitude warming
448 and contraction of the SPV are observed (Fig 3).

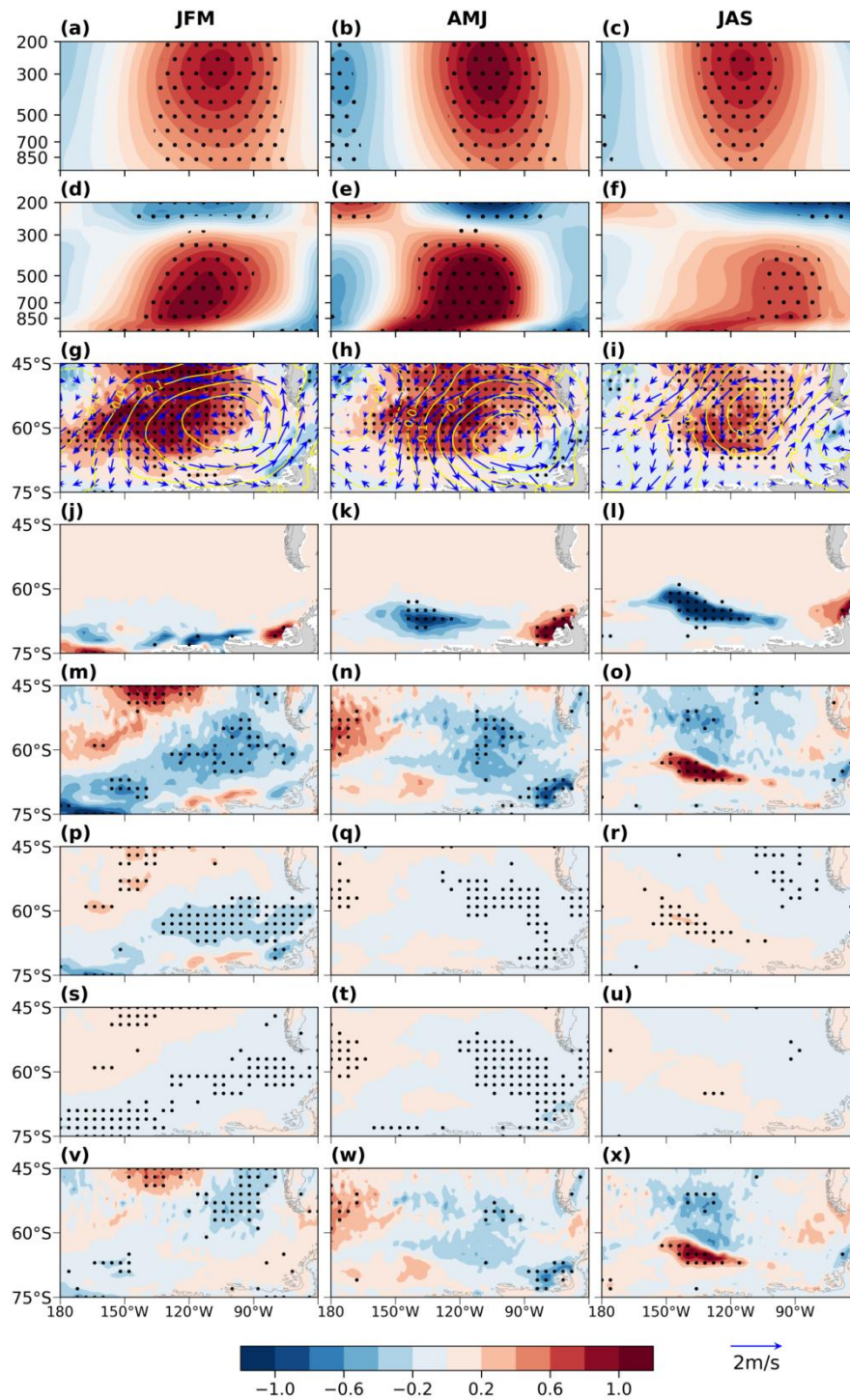
449 This relationship is reversed under cold Niño 4 SSTa conditions. Specifically, when cold
450 SSTa occur in the central tropical Pacific, planetary wave activity and their associated
451 disturbances to the stratosphere are suppressed, leading to polar stratospheric cooling and a
452 extended SPV.

453 **4.2 Mid-latitude sea-air interactions**

454 **4.2.1 Ocean responses**

455 The Niño 4 SSTa influence mid-latitude ocean temperatures through atmospheric
456 teleconnections. During JFM, a positive Niño 4 SSTa trigger a PSA teleconnection pattern,
457 resulting in a positive geopotential height anomaly centered near 110 °W, 60 °S over the
458 southeastern Pacific (Figs. 5j and 7g). The associated poleward surface winds and adiabatic

459 subsidence warm the lower troposphere (Figs. 8a,d). Therefore, the ocean will gain heat, as
 460 indicated by the negative net heat flux anomaly, leading to a localized SST warming (Fig. 8g).
 461 Here net heat flux is defined as the sum of latent and sensible heat fluxes, long-wave radiation
 462 and short-wave radiation (Fig. 8m). Simultaneously, there is a modest reduction in SIC in the
 463 Amundsen and Ross Seas (Fig. 8j).
 464



465
 466 **Figure 8.** Composite differences between warm and cold Niño 4 years. The panels show three-month means

467 for January–March (left column), April–June (middle column), and July–September (right column). (a–c)
 468 Geopotential heights (shaded, unit: 5 dagpm), averaged over 45 °S–75 °S, (d–f) temperatures (shaded, unit: K),
 469 averaged over 45 °S–75 °S, (g–i) SST (shaded, unit: K), SLP (contours, unit: 1000 Pa), and 10-meter winds
 470 (vector, unit: 2 m/s), (j–l) sea ice concentration (SIC, unit: 30 %), (m–o) net upward total heat flux (the sum of
 471 turbulence heat flux, upward long-wave heat flux and net downward short-wave radiation, shaded, unit: 3
 472 W/m²), (p–r) net downward short-wave radiation (shaded, unit: 3 W/m²), (s–u) upward long-wave radiation
 473 (shaded, unit: 3 W/m²), and (v–x) turbulence heat flux (the sum of latent and sensible heat flux; shaded, unit: 3
 474 W/m²). Black dots indicate regions statistically significant at the 95% confidence level.

475

476 A similar pattern persists during AMJ (Figs. 8b,e). The PSA pattern associated with warm
 477 Niño 4 SSTa remains evident (Fig. 5k), although the area of negative net heat flux contracts (Fig.
 478 8n), and continues to support warming SST in the southeastern Pacific through ongoing sea–air
 479 heat exchange (Fig. 8h). As a result, SIC in the Amundsen and the Ross Seas declines further (Fig.
 480 8k). Additionally, sustained tropospheric warming enhances geopotential height anomalies in
 481 both the troposphere and lower stratosphere (Figs. 8b,e).

482 **4.2.2 Ocean feedback to the atmosphere**

483 The tropospheric warming center is located between 500 hPa and 850 hPa during JFM and
 484 AMJ, while the maximum warming shifts below 850 hPa in JAS, suggesting an enhanced
 485 influence from the ocean surface (Figs. 8d-f). During JAS, Niño 4 SST anomalies weaken (Fig.
 486 5c), indicating a reduced influence of tropical central Pacific SST forcing. Nevertheless, owing to
 487 the ocean’s large heat capacity, warm SST anomalies in the southeastern Pacific persist (Fig. 8i).
 488 As the amplitude of Niño 4 SST anomalies declines, the accumulated heat in the southeastern
 489 Pacific is gradually released (Fig. 8o). This heat is transported upward by atmospheric transient
 490 eddies and planetary waves generated by enhanced local baroclinicity in the lower troposphere,
 491 thereby influencing upper-atmospheric circulation (Nakamura et al., 2008; Sampe et al., 2010).
 492 Consequently, a pronounced positive geopotential height anomaly associated with the PSA
 493 pattern persists over this region (Fig. 5l).

494 During JAS, surface net heat flux is largely driven by sea-ice loss in the Amundsen and Ross
 495 Seas (Figs. 8l,o). Specifically, the sustained warm SSTa drive substantial sea-ice loss.
 496 Comparison between surface heat flux (Fig.8o) and SIC (Fig.8l) shows sea-ice loss has a
 497 pronounced impacts on surface heat flux. During JAS, solar short-wave radiation reaches its
 498 minimum, and its contribution to the net heat flux is relatively small (Fig. 8r). Meanwhile, the
 499 contribution from longwave radiation also is relatively weak (Fig. 8u). The primary contributions
 500 come from turbulence heat fluxes (Fig. 8x) and temperature advection (Fig 8i).

501 During this stage, northerly anomalies dominate the region over 40 °S–60 °S, 90 °W–140 °W,
502 which transport warm air advection from tropical regions to the mid–latitudes and enhance ocean
503 heat uptake from atmosphere. Although the negative net heat flux anomalies persist north of
504 60 °S, their intensity is relatively weak. In contrast, significant oceanic heat is released to the
505 atmosphere in the regions where sea-ice has retreated (Fig. 8o), warming the lower troposphere
506 (Fig. 8f). In addition, the enhanced heat in the lower troposphere is transported upward,
507 sustaining the positive geopotential height anomaly through the upward displacement of isobaric
508 surfaces (Fig. 8c), consistent with previous studies (Honda et al., 2009; Kim et al., 2014; Yang et
509 al., 2016; Hoshi et al., 2017).

510 Moreover, near-surface heating associated with sea-ice loss acts as an effective source of
511 planetary wave under wintertime background conditions, contributing to the amplification of
512 zonal wave patterns and enhanced planetary wave propagation (Kim et al., 2014; Nakamura et al.,
513 2015). Notably, while net heat flux is dominated by ocean heat uptake during JFM and AMJ, the
514 influence of sea-ice loss becomes predominant in JAS, resulting in net heat release from the
515 ocean to the atmosphere (Figs. 8m-o). This positive feedback reinforces the Southern Hemisphere
516 zonal-wave pattern and amplifies the planetary wave anomalies (Zi et al., 2025). Recent modeling
517 studies also suggest that sea-ice loss in the Amundsen Sea and the broader Antarctic region can
518 have pronounced impacts on the SPV (Song et al., 2025). The sea-ice loss tends to sustain the
519 influence of the Niño 4 SSTa on stratospheric temperatures during JAS by enhancing surface heat
520 fluxes (Fig.8).

521 **4.3 Ozone transport**

522 The enhanced planetary wave associated with the warm Niño 4 SSTa not only warms the
523 polar stratosphere but also significantly alters the B–D circulation and polar ozone transport
524 (Wang et al., 2025). Figures 7d–f present the composite differences in the zonal-mean residual
525 circulation and ozone mass mixing ratio between warm and cold Niño 4 years, each averaged
526 over three–month periods from January to September of the following year.

527 During JFM, convective anomalies in the tropical Pacific Ocean drive changes in the
528 residual circulation (Fig. 5d), resulting in decreases to the ozone mass mixing ratio in the tropical
529 lower stratosphere and increased values in the mid–latitude lower stratosphere (Fig. 7d). However,
530 upward–propagating planetary waves are largely confined below 50 hPa in the mid– and

531 low-latitude (Fig. 7a), strengthening the residual circulation primarily north of 60 °S. As a result,
532 ozone transport to higher altitudes and into the polar region remains limited (Fig. 7d). In AMJ,
533 although convective anomalies in the tropical Pacific Ocean persist and planetary wave increases
534 in the upper stratosphere (Fig. 7b), many of the waves are refracted equatorward, resulting in only
535 modest polar ozone transport (Fig. 7e). In JAS, however, upward-propagating planetary waves
536 are strongly refracted toward mid- and high-latitude, enhancing the residual circulation and
537 promoting both poleward and upward ozone transport (Fig. 7f). The increased poleward ozone
538 transport enhances solar radiation absorption, playing an important role in the polar stratospheric
539 warming through dynamical-chemical coupling (Solomon et al., 2016). In addition, adiabatic
540 warming associated with descending air in the residual circulation further contributes to the
541 stratospheric warming over the polar region.

542

543 **5 Multivariate regression model**

544 The preceding analyses reveal that boreal winter Niño 4 SSTa exert a significant lagged
545 influence on the Antarctic stratospheric circulation during the subsequent austral winter. This
546 finding has important implications for the seasonal prediction of stratospheric variability.
547 However, although the boreal winter Niño 4 index is significantly correlated with
548 July–September mean T_{10-30} index, it accounts for only 18.5 % of the variance in stratospheric
549 temperature ($R^2 = 0.185$). To better interpret variability in the Antarctic stratosphere, additional
550 factors need to be considered.

551 Previous studies found that the PSA teleconnection associated with the Niño 4 SSTa is a key
552 mechanism influencing the Antarctic stratosphere. The PSA pattern is represented by the second
553 EOF mode of monthly SLP anomalies (Fig. 9). The corresponding PSA index is defined as the
554 time series of this EOF mode. During boreal winter, the PSA index is significantly simultaneous
555 correlated with the Niño 4 index ($R = 0.40$, $p < 0.01$), suggesting that the Niño 4 SSTa modulate
556 the PSA pattern. However, the correlation between the June PSA index and the boreal winter
557 Niño 4 index is relatively weak ($R = 0.28$, $p < 0.05$). In addition, the June PSA index is
558 significantly correlated with May–June mean Antarctic sea-ice ($R = 0.49$, $p < 0.01$), suggesting
559 that the June PSA pattern may be maintained by sea-ice anomalies and other factors. Furthermore,

560 correlating the PSA index from December to the following September with the July–September
 561 mean T_{10-30} index shows that the June PSA index exhibits the strongest correlation (Table 3, $R =$
 562 $0.47, p < 0.01$).

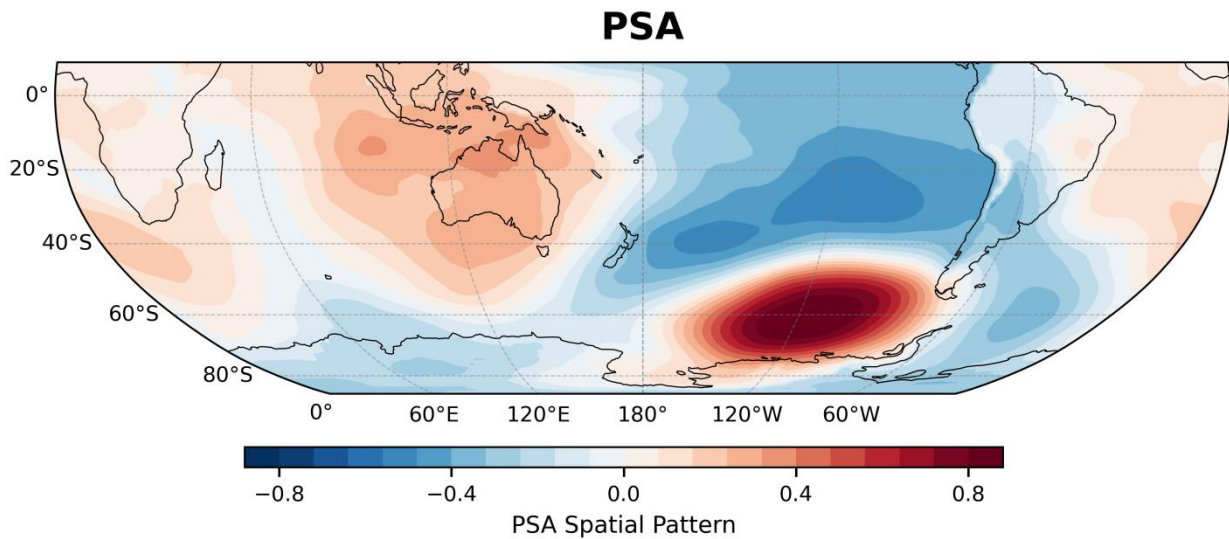
563

564 **Table 3.** Correlation coefficients between July–September mean T_{10-30} index and SIC index (SIC_{AR}) over the
 565 Amundsen and Ross Seas (averaged over $180^\circ W-90^\circ W$), SST index over the South Pacific (SST_{SP}) and PSA
 566 index.

	SIC_{AR}	SST_{SP}	PSA
Jan	-0.18	0.25	0.32**
Feb	-0.08	0.27*	0.21
Mar	-0.18	0.29*	0.28*
Apr	-0.24	0.30**	-0.12
May	-0.38***	0.27*	0.10
Jun	-0.44***	0.32**	0.47***
Jul	-0.23	0.30**	0.03
Aug	-0.28*	0.30**	0.29*
Sep	-0.31**	0.29*	0.05

567 Note: Colors and asterisks denote statistical significance: red with *** for the 99 % confidence level,
 568 green with ** for 95 %, and magenta with * for 90 %.

569



570

571 **Figure 9.** PSA teleconnection pattern represented by the second EOF mode of monthly SLP.

572

573 As a result, a multivariate linear regression (MLR) model is used to quantitatively assess the
 574 linear relationship between the stratospheric temperature index (T_{10-30}) and potential factors
 575 including the Niño 4 and PSA indices. We have

576
$$T_{10-30} = \beta_0 + \beta_1 Ni\tilde{n}o4 + \beta_2 PSA + \varepsilon \quad (9)$$

577 where β_0 is the intercept, β_1 , β_2 are the regression coefficients associated with each
 578 factor, and ε denotes the residual error term. Prior to the regression analysis based on Eq. (9), all
 579 input time series are standardized. The regression analysis is performed using MATLAB's fitlm
 580 function, which yields estimates of regression coefficients, standard errors, t-statistics, and
 581 p-values, along with overall model diagnostics, such as the coefficient of determination (R^2) and
 582 the F-statistic. To evaluate the significance of individual factors, three confidence levels are
 583 adopted: 90 %, 95 %, and 99 %, corresponding to p-value thresholds of 0.1, 0.05, and 0.01,
 584 respectively. Factors with p-values below these thresholds are considered statistically significant.
 585 The overall performance and goodness-of-fit of the model are assessed using the R^2 metric.

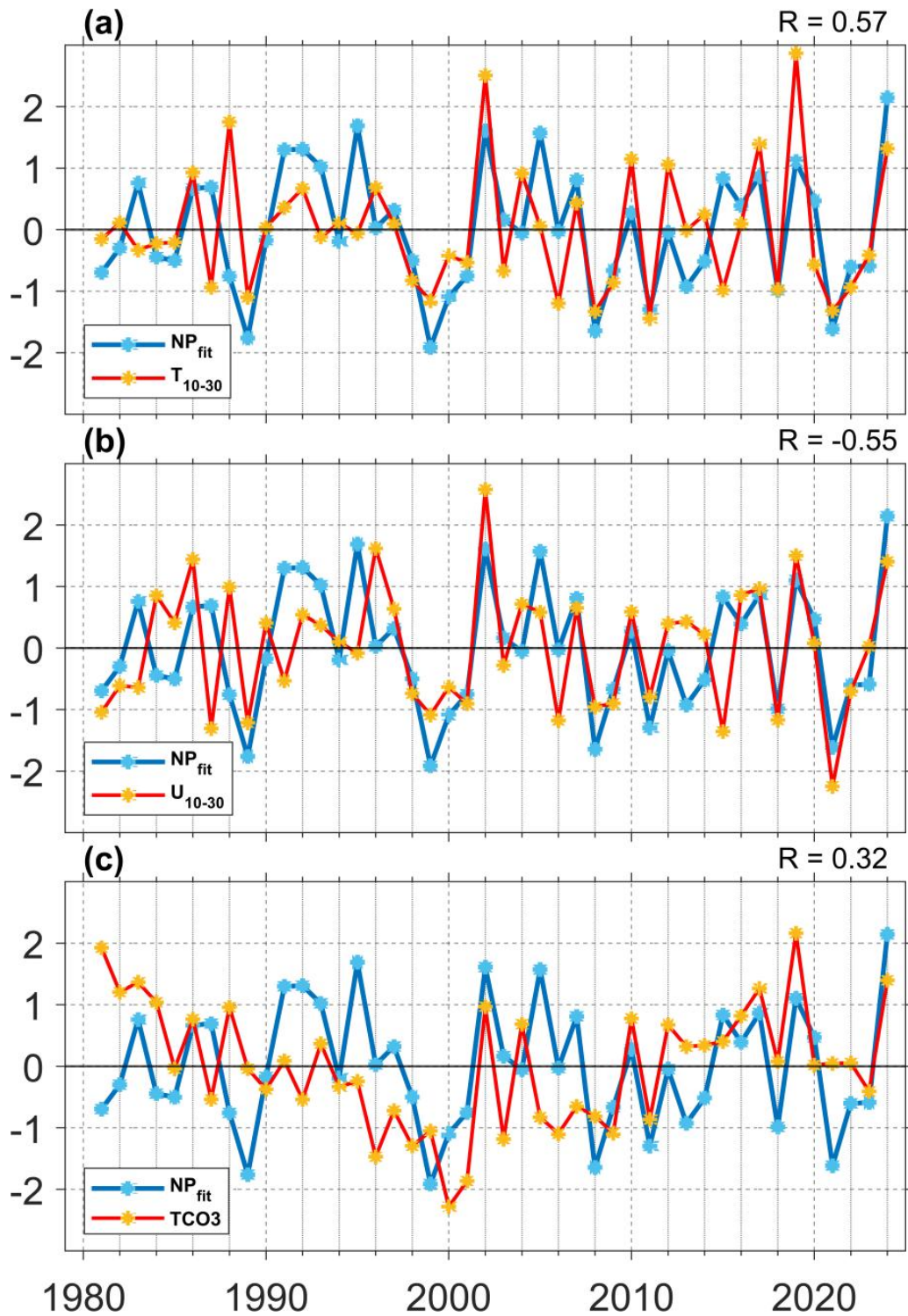
586 To predict the July–September mean T_{10-30} index, the boreal winter Niño 4 (Niño 4_{DJF}) index
 587 and the June PSA (PSA_{Jun}) index are used as factors in Eq. (9). We yield

588
$$T_{10-30} = 0.324 Ni\tilde{n}o4_{DJF} + 0.384 PSA_{Jun} + \varepsilon \quad (10)$$

589 with $\beta_0 = 0$. This linear regression model yields a coefficient of determination (R^2) of
 590 0.321, indicating that the factors collectively explain approximately 32 % of the variance in the
 591 July–September mean T_{10-30} index. The model's F-statistic is 9.71 with a corresponding p-value
 592 of 0.00035, which is significant at the 99 % confidence level. Among the factors, the Niño 4_{DJF}
 593 and PSA_{Jun} exhibit statistically significant regression coefficients ($p = 0.0201$ and $p = 0.0065$,
 594 respectively), confirming their primary roles in modulating stratospheric temperature variability.

595 To assess model performance, the regression–based fitted index (referred to as NP_{fit}) was
 596 compared with observed July–September mean T_{10-30} , U_{10-30} , and TCO_3 (Fig. 10). The NP_{fit} index
 597 shows significant correlation with observed values for T_{10-30} ($R = 0.57$, $p < 0.01$), U_{10-30} ($R =$
 598 -0.55 , $p < 0.01$), and TCO_3 ($R = 0.32$, $p < 0.05$), all of which exceed the corresponding
 599 correlation values ($R = 0.4$, -0.38 and 0.36) obtained using the Niño 4 index alone (Fig. 2). While
 600 the boreal winter Niño 4 index plays a key role in Antarctic stratospheric temperature variability,
 601 incorporating the June PSA index further improves the explanation of this variability. This
 602 underscores the importance of both tropical forcing and extratropical feedback processes in
 603 modulating polar stratospheric circulation.

604



605
 606 **Figure 10.** Time series of the standardized NP_{fit} index (blue line), along with (a) July–September mean T₁₀₋₃₀
 607 index (red line), (b) July–September mean U₁₀₋₃₀ index (red line, multiplied by -1), and (c) July–September
 608 mean TCO₃ index (red line) from 1981 to 2024. R in the upper right corner is the correlation coefficient
 609 between NP_{fit} index and T₁₀₋₃₀, U₁₀₋₃₀, and TCO₃ indices, respectively.

610

611 6 CMIP6 results

612 To further assess the cross-seasonal effects of tropical central Pacific SSTa on Antarctic

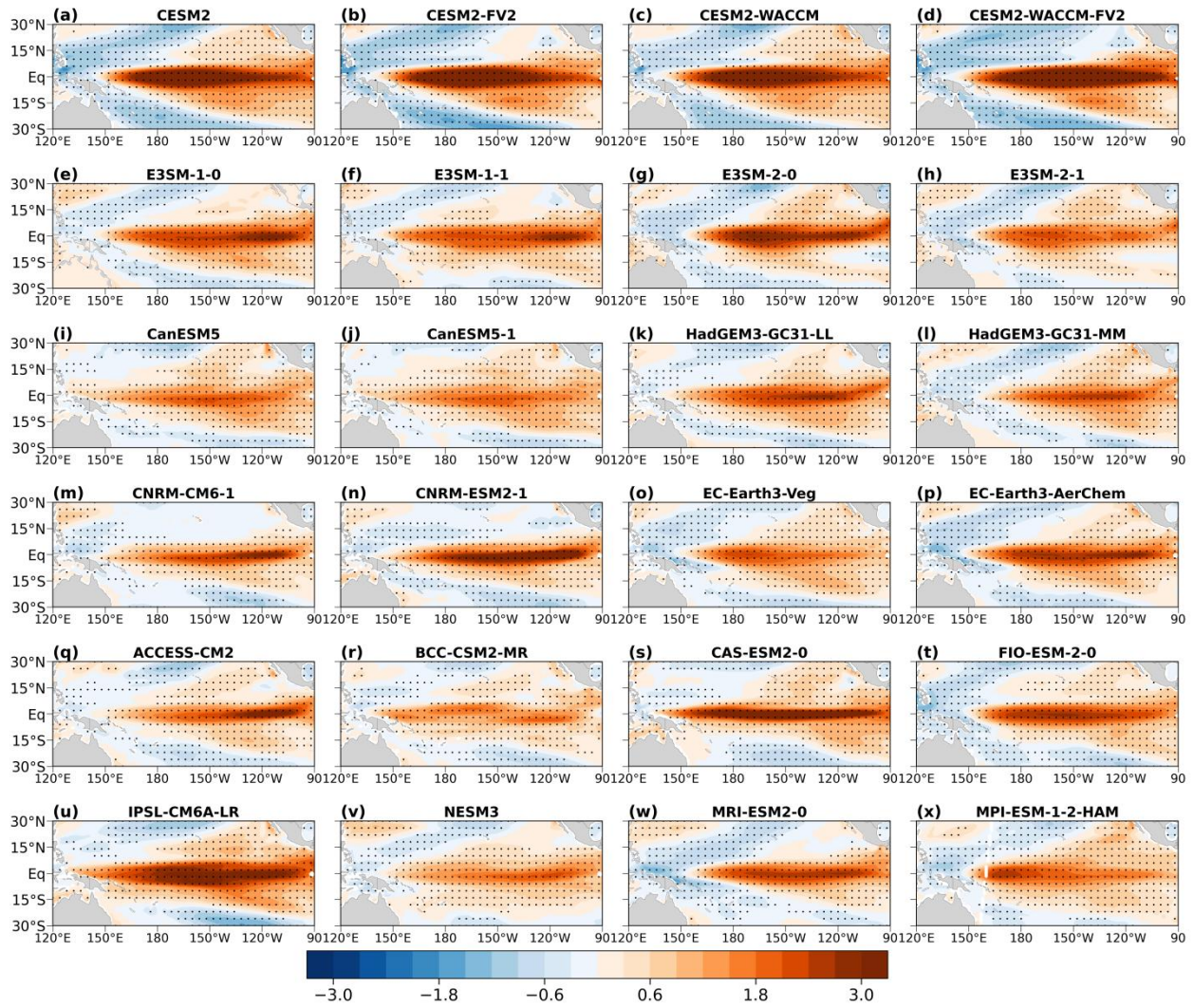
613 stratospheric temperature anomalies, we analyze 24 CMIP6 historical fully coupled model
614 simulations covering the period 1951–2014. For each model, the Niño 4 index is first calculated
615 following the same procedure as used for the observational analysis. Warm and cold Niño 4 years
616 are then identified using a threshold of $\pm 0.5\sigma$. Composite differences between warm and cold
617 years are subsequently constructed for DJF mean SST (Fig. 11), JAS mean temperatures at 10
618 hPa (Fig. 12), JAS mean SST (Fig. 13), and JAS mean Antarctic SIC (Fig. 14).

619 In the DJF mean SST, significant warm SSTa consistently emerge over the tropical central
620 Pacific in all models (Fig. 11). Consistent with the observational results, warm SSTa over the
621 tropical central Pacific during the boreal winter are significantly associated with Antarctic
622 stratospheric warming in the subsequent austral winter (Fig. 12). Although the magnitude of the
623 JAS mean Antarctic stratospheric warming at 10 hPa varies among models, for example,
624 relatively stronger warming is simulated in CanESM5, CanESM5-1, HadGEM3-GC31-LL,
625 ACCESS-CM2, and MPI-ESM-1-2-HAM (Figs. 12i,j,k,q,x), whereas weaker warming is evident
626 in models such as E3SM-1-1, CNRM-CM6-1, and EC-Earth3-Veg (Figs. 12f,m,o). Nevertheless,
627 most models exhibit statistically significant warm anomalies. Moreover, consistent with the
628 observations, the warming signal in most models is predominantly located over the Eastern
629 Hemisphere (Fig. 12 and Figs.3 b-d), with only a few models (e.g., CNRM-CM6-1,
630 FIO-ESM-2-0, and MRI-ESM2-0) showing maxima over the Western Hemisphere (Figs.
631 12m,t,w).

632 In addition, the July-September mean SST exhibit a statistically significant positive
633 anomalies over the southeastern Pacific (Fig. 13). Similarly, Antarctic SIC shows pronounced
634 negative anomalies over the Amundsen Sea and Ross Sea sectors (Fig. 14), indicating reduced
635 sea-ice concentration. Although a small number of models (e.g., E3SM-2-0, BCC-CSM2-MR,
636 and MPI-ESM-1-2-HAM) display relatively weaker sea-ice loss (Figs. 14g,r,x), the overall
637 response is consistent across models.

638 Therefore, these results are consistent with observations and support the presence of a
639 cross-seasonal linkage between tropical central Pacific SST anomalies and Antarctic stratospheric
640 polar temperatures.

641



642

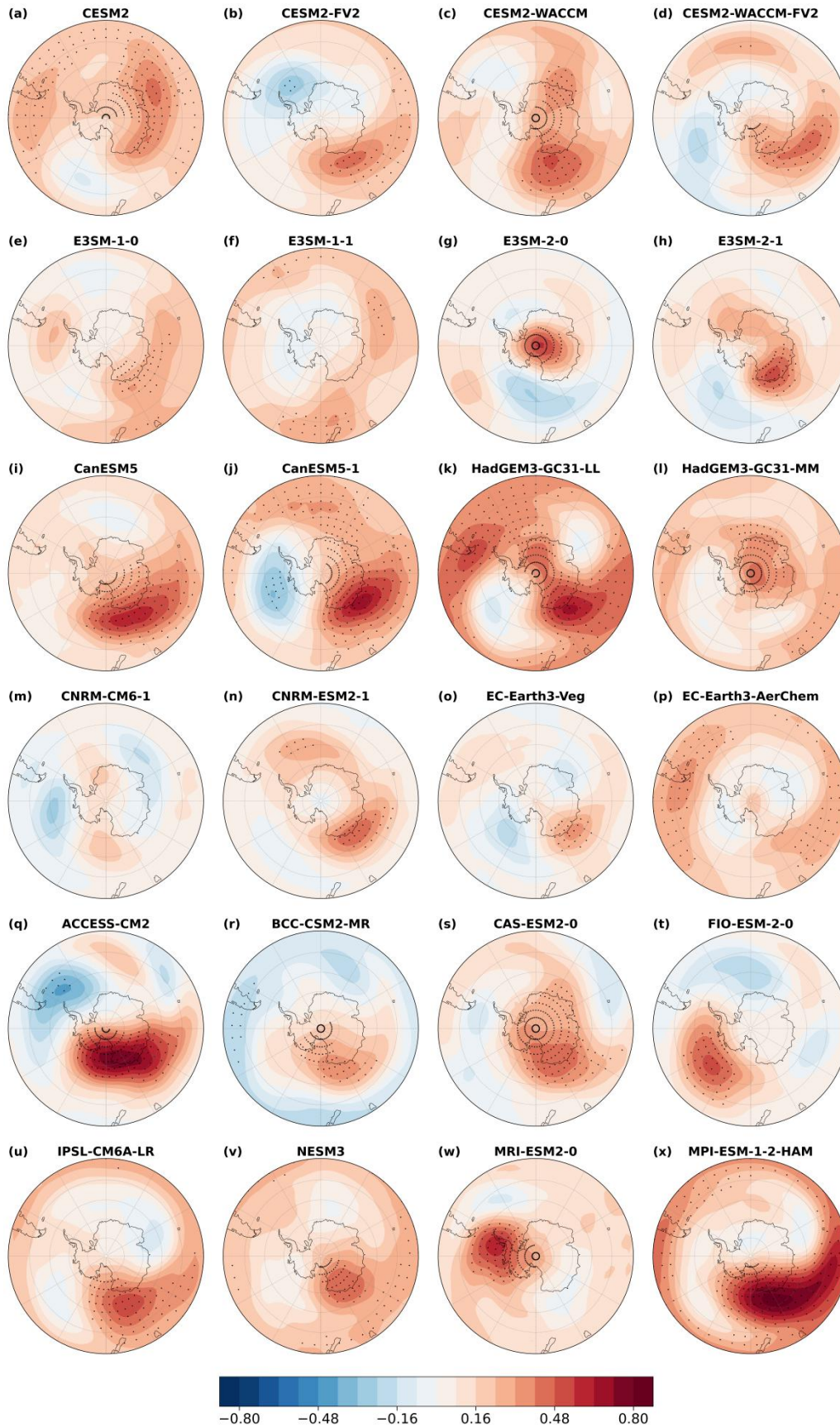
643

644

645

646

Figure 11. Composite differences in December–February mean SST (shaded, unit: K) between warm and cold Niño 4 years in 24 CMIP6 experiments. Black dots indicate regions statistically significant at the 95% confidence level.



647

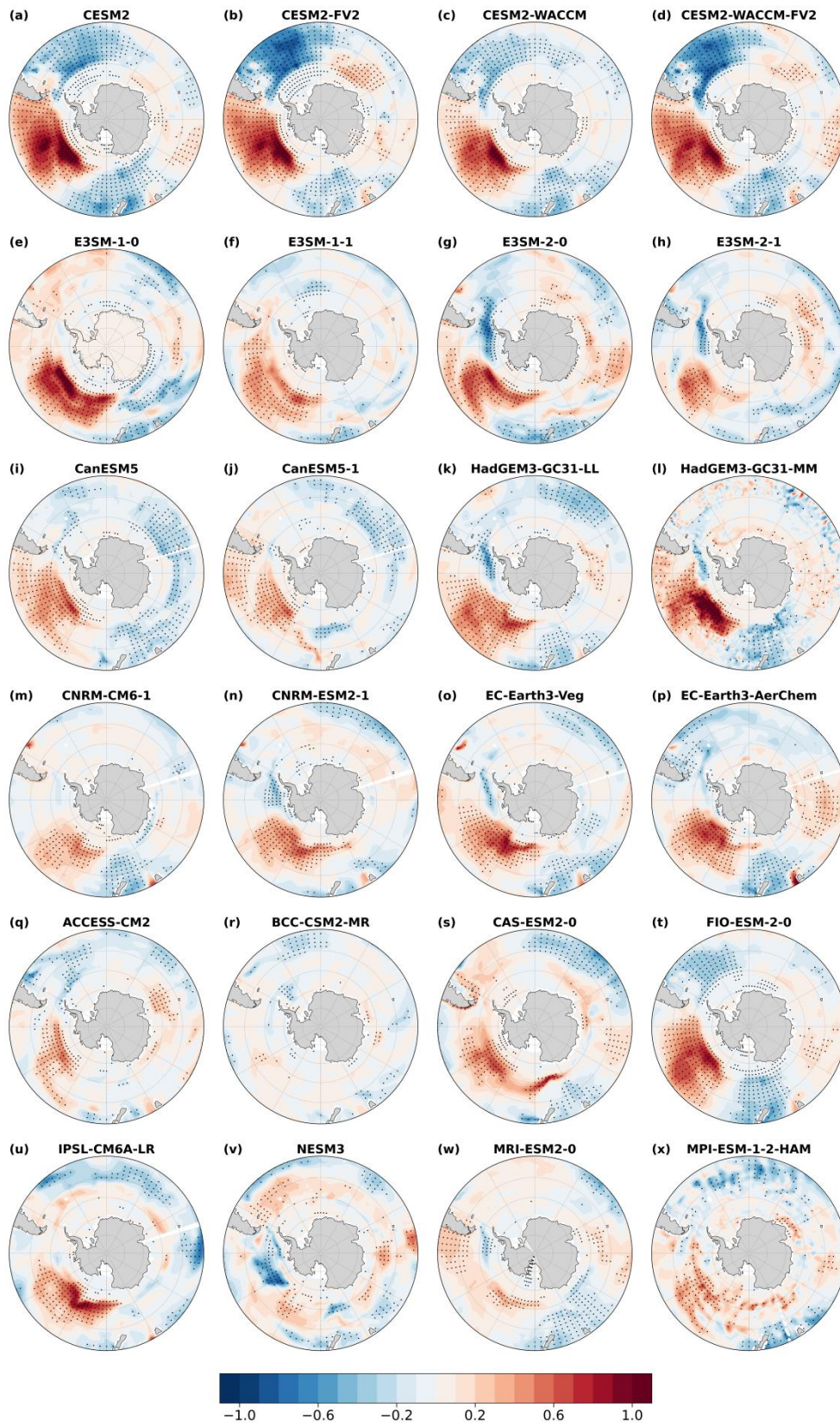
648

649

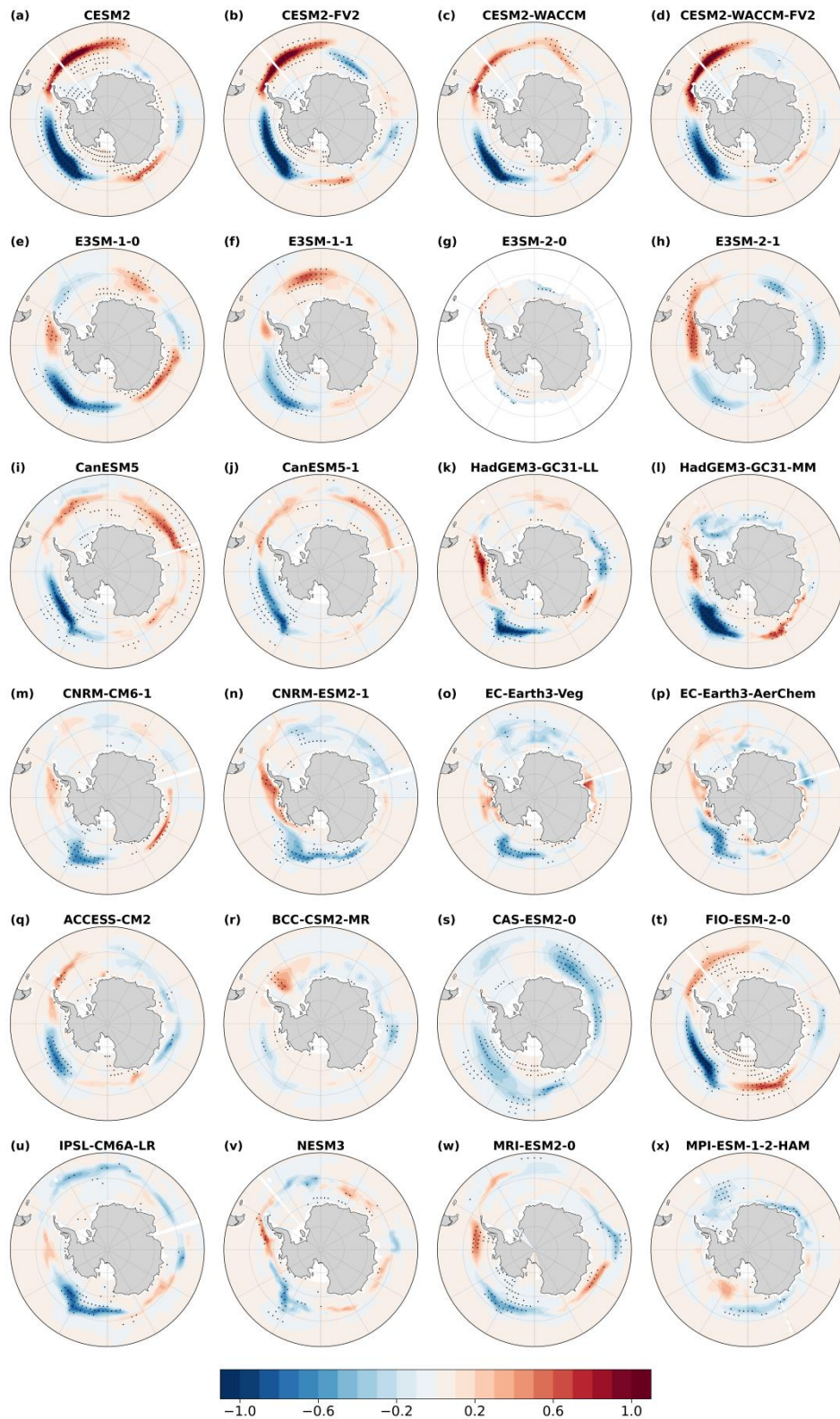
650

Figure 12. Composite differences in July–September mean temperature (shaded, unit: K) over the 10 hPa between warm and cold Niño 4 years in 24 CMIP6 experiments. Black dots indicate regions statistically significant at the 95% confidence level.

651



652
 653 **Figure 13.** Composite differences in July–September mean SST (shaded, unit: K) between warm and cold Niño
 654 4 years in 24 CMIP6 experiments. Black dots indicate regions statistically significant at the 95% confidence
 655 level.



656

657 **Figure 14.** Composite differences in July–September mean SIC (shaded, unit: 30 %) between warm and cold
 658 Niño 4 years in 24 CMIP6 experiments. Black dots indicate regions statistically significant at the 95%
 659 confidence level.

660

661

662

663 **7 Conclusions and discussions**

664 The cross–seasonal influence of the tropical central Pacific sea surface temperature (SST) on
665 Antarctic stratospheric circulation was investigated in this study using ERA5 reanalysis of 45
666 years (1980–2024). Our analysis revealed that warm (cold) SSTa in the Niño 4 region (Central
667 Pacific) during the boreal winter are followed by significantly warming (cooling) of the Antarctic
668 stratosphere in the subsequent austral winter (July–September), accompanied by a contracted
669 (expanded) stratospheric polar vortex (SPV). Among the ENSO indices (Niño 3, Niño 3.4, Niño
670 4), the boreal winter Niño 4 index exhibits the strongest and most robust correlation with the
671 July–September polar stratospheric temperature (T_{10-30}) index, reaching $R \approx 0.43$ ($p < 0.01$). In
672 contrast, correlations with the Niño 3.4 and Niño 3 indices (Eastern Pacific) are substantially
673 weaker, suggesting that the Niño 4 SSTa are the primary drivers of the observed Antarctic
674 stratospheric responses. In addition to the observational analyses, the fully coupled simulations
675 from 24 CMIP6 models also reproduce the cross–seasonal connection between tropical central
676 Pacific SSTa and Antarctic stratospheric temperature anomalies, providing further evidence for
677 the robustness of this teleconnection.

678 In this study, the tropical central Pacific SST and the Antarctic stratospheric indices both
679 exhibit notable variance on decadal timescales (Fig. 4a). To account for the influence of the
680 decadal variability, a 10-year low-pass filter was applied to both the Niño 4 and the T_{10-30} indices
681 to isolate their decadal components (Fig. 15a). The interannual components were then obtained
682 by subtracting the decadal signals from the original time series (Fig. 15b). The decadal
683 components exhibit a much stronger correlation of 0.82 ($p < 0.01$), indicating that a pronounced
684 decadal-scale relationship exists between the two indices. Importantly, the interannual
685 components also remain significantly correlated, with a correlation coefficient of 0.41 ($p < 0.01$).
686 Although this value is slightly lower compared to that of the original series (Fig. 4a), it remains
687 statistically robust, demonstrating the tropical central Pacific SST exerts a significant influence
688 on Antarctic stratospheric temperatures events at interannual timescales.

689 The underlying dynamics involve the Pacific–South America (PSA) teleconnection pattern
690 triggered by the Niño 4 SSTa and mediated through wave-mean flow interactions. During boreal
691 winter, warm SSTa in the Niño 4 region enhance convection near the dateline, exciting a Rossby
692 wave train that propagates poleward and eastward across the Southern Hemisphere. This wave

693 activity generates a positive geopotential height anomaly over the southeastern South Pacific and
694 a negative anomaly over the South Atlantic, reinforcing the climatological wave-1 ridge and
695 trough structure. As the seasonal transition into austral summer and winter progresses, the
696 Antarctic stratospheric circulation shifts toward a more westerly regime, creating favorable
697 conditions for planetary waves into the polar stratosphere. The convergence of Eliassen–Palm
698 (E–P) flux, followed by wave breaking, induces stratospheric warming and a deceleration of the
699 SPV.

700 It was also found that warm SSTa in the South Pacific and sea-ice loss over the Amundsen
701 and Ross Seas can reinforce the mid- and high-latitude zonal wave train through sea–air
702 interactions. Specially, PSA teleconnection associated with the Niño 4 warming drives ocean heat
703 uptake and rising SSTa in the southeast Pacific from January–March to April–June. With
704 progression of seasons, this remote forcing weakens during June–September, a local sea–air
705 feedback becomes dominant, persistent warm waters accelerate sea-ice melt, and the subsequent
706 oceanic heat release sustains the atmospheric positive height anomaly, thereby strengthening the
707 planetary wave anomaly.

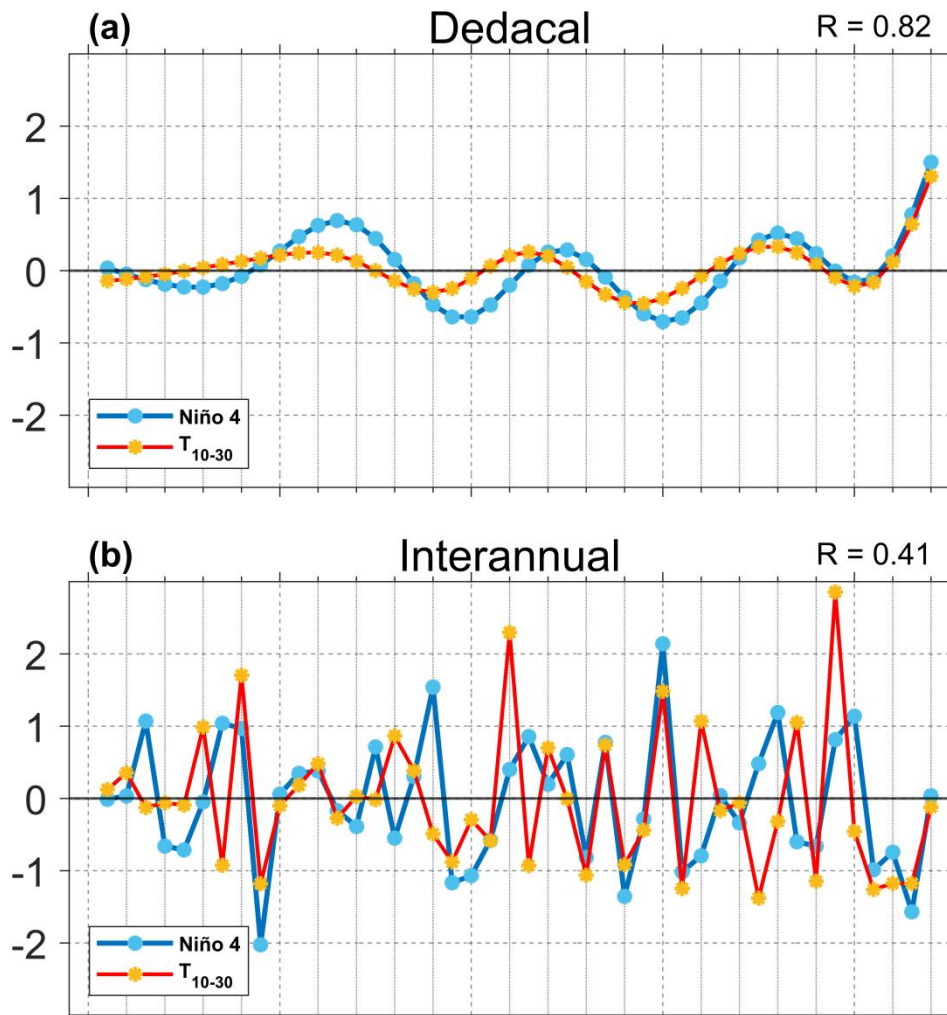
708 Furthermore, stronger planetary wave anomalies induced by warm Niño 4 SSTa were found
709 to play a crucial role in modulating Antarctic ozone transport. These anomalous waves enhance
710 the Brewer–Dobson circulation, facilitating the ozone transport from the tropics to the polar
711 stratosphere and leading to elevated ozone concentrations over Antarctica. The increased ozone
712 concentrations enhance ultraviolet absorption, further amplifying stratospheric warming.
713 Simultaneously, a warmer stratosphere inhibits the formation of polar stratospheric clouds (PSCs),
714 thereby suppressing the heterogeneous chemical reactions responsible for ozone depletion and
715 mitigating Antarctic ozone loss (Solomon et al., 2016).

716 To synthesize these processes, Figure 16 provides a schematic representation of the
717 proposed physical mechanism. It illustrates how boreal winter Niño 4 SST anomalies initiate a
718 chain of dynamical and thermodynamical responses, including tropical convection, the PSA
719 teleconnection, planetary wave propagation, mid-latitude air–sea feedbacks, enhanced
720 Brewer–Dobson circulation, and ozone transport, which together lead to Antarctic stratospheric
721 warming in the subsequent austral winter.

722 A multivariate regression statistical model was used in this study to determine the linear

723 relationship between stratospheric temperature variations and Niño 4 SSTa. The boreal winter
 724 Niño 4 index alone accounts for approximately 18 % of the variance in July–September polar
 725 stratospheric temperatures. However, when the June PSA index is included as additional factor,
 726 the explained variance nearly doubles to 32 %. This highlights the combined importance of both
 727 tropical forcing and mid–latitude atmospheric responses in stratospheric temperature variability.
 728 Nonetheless, a substantial portion of stratospheric variability remains unexplained. This reflects
 729 the influence of atmospheric internal dynamics, as well as contributions from other drivers such
 730 as the Quasi–Biennial Oscillation (QBO), solar activity, and mid–latitude tropospheric wave
 731 sources. Additional factors may be identified through a range of approaches, including numerical
 732 modeling, machine learning, and causal inference.

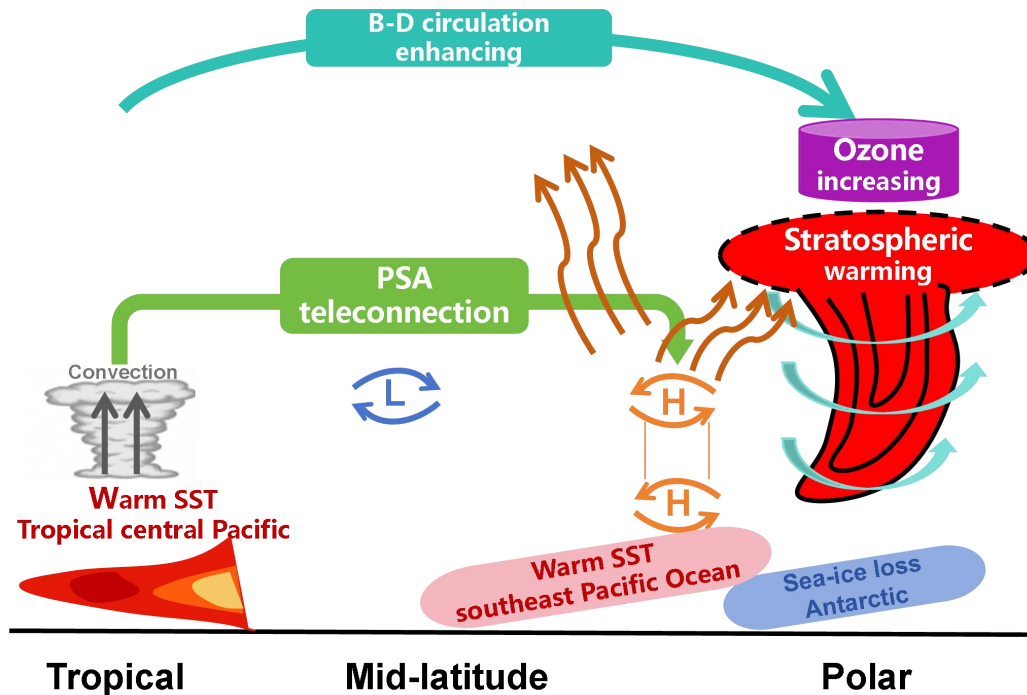
733



734

735 **Figure 15.** Time series of standardized Niño 4 index (blue line) and the July–September mean T_{10-30} index (red
 736 line). (a) and (b) show the decadal and interannual components, respectively. The value R in the upper right
 737 corner denotes the correlation coefficient between the Niño 4 and the T_{10-30} indices.

738



739

740 **Figure 16.** Schematic diagram of the proposed physical mechanism linking boreal winter Niño 4 SST

741 anomalies to austral winter Antarctic stratospheric warming.

742

743 **Code and data availability.**

744 The ERA5 reanalysis data are available from the European Centre for Medium-Range
 745 Weather Forecasts at Hersbach et al. (2023). The Niño 4 index came from National Oceanic and
 746 Atmospheric Administration (<https://psl.noaa.gov/data/timeseries/month/DS/Nino4/>,
 747 <https://psl.noaa.gov/data/timeseries/month/DS/Nino3/>, and
 748 <https://psl.noaa.gov/data/timeseries/month/DS/Nino34/>). The code used in this article is
 749 accessible from the corresponding author.

750

751 **Author contributions**

752 YZ, ZL, JS, and ZX contributed to the conceptualization of the study. YZ designed the
 753 methodology, developed the software, performed the validation, formal analysis, investigation,
 754 data curation, and visualization. JS, GL, and ZX were responsible for funding acquisition, project
 755 administration, and providing the necessary resources. The work was supervised by ZL, JS, GL,
 756 WP, and ZX. YZ prepared the original manuscript with contributions from ZL, JS, WP, and ZX.
 757 All authors contributed to the review and editing of the final manuscript.

758

759 Competing interests

760 The contact author has declared that none of the authors has any competing interests.

761

762 Acknowledgments

763 The research was supported by the National Natural Science Foundation of China
764 (42394123 and 42394122), “Transforming Climate Action” program
765 (TCA-LRP-20240B-1.1-WP6JS) led by Dalhousie University (Halifax, Canada), Natural
766 Sciences and Engineering Research Council of Canada to JS (NSERC, Grant NOs: 217081),
767 Gansu Provincial Natural Science Foundation (25JRRA323), and the China Scholarship Council
768 (CSC, 202306340119). We also appreciate all the support provided by the Department of
769 Oceanography, Dalhousie University.

770

771 Financial support

772 This research was supported by the National Natural Science Foundation of China
773 (42394123 and 42394122), the “Transforming Climate Action” program
774 (TCA-LRP-20240B-1.1-WP6JS), Natural Sciences and Engineering Research Council of Canada
775 to JS (NSERC, Grant NOs: 217081), Gansu Provincial Natural Science Foundation (25JRRA323),
776 and the China Scholarship Council (CSC, 202306340119).

777

778 **References**

- 779 Albers, J.R. and Birner, T.: Vortex Preconditioning due to Planetary and Gravity Waves prior to
780 Sudden Stratospheric Warmings, *Journal of the Atmospheric Sciences*, 71, 4028–4054,
781 <https://doi.org/10.1175/jas-d-14-0026.1>, 2014.
- 782 Alexander, M.A., Bladé, I., Newman, M., Lanzante, J. R., Lau, N. C., and Scott, J. D.: The
783 Atmospheric Bridge: The Influence of ENSO Teleconnections on Air–Sea Interaction over
784 the Global Oceans, *Journal of Climate*, 15, 2205–2231,
785 [https://doi.org/10.1175/1520-0442\(2002\)015<2205:tabtio>2.0.co;2](https://doi.org/10.1175/1520-0442(2002)015<2205:tabtio>2.0.co;2), 2002.
- 786 Andrews, D. G. and McIntyre, M. E.: An exact theory of nonlinear waves on a Lagrangian-mean
787 flow, *Journal of Fluid Mechanics*, 89, 609–646, <https://doi.org/10.1017/s0022112078002773>,
788 1978.
- 789 Andrews, D. G. and McIntyre, M. E.: Planetary Waves in Horizontal and Vertical Shear: The
790 Generalized Eliassen-Palm Relation and the Mean Zonal Acceleration, *Journal of the*
791 *Atmospheric Sciences*, 33, 2031–2048,
792 [https://doi.org/10.1175/1520-0469\(1976\)033<2031:pwhav>2.0.co;2](https://doi.org/10.1175/1520-0469(1976)033<2031:pwhav>2.0.co;2), 1976.
- 793 Andrews, D. G., Holton, J. R., and Leovy, C. B.: *Middle atmosphere dynamics*, Academic Press,
794 San Diego, 489 pp, <https://doi.org/10.1002/qj.49711548612>, 1987.
- 795 Baldwin, M. P. and Dunkerton, T. J.: Stratospheric Harbingers of Anomalous Weather Regimes,
796 *Science*, 294, 581–584, <https://doi.org/10.1126/science.1063315>, 2001.
- 797 Baldwin, M. P., Ayarzagüena, B., Birner, T., Butchart, N., Butler, A. H., Charlton - Perez,
798 AndrewJ., Domeisen, DanielaI. V., Garfinkel, ChaimI., Garny, H., Gerber, EdwinP., Hegglin,
799 MichaelaI., Langematz, U., and Pedatella, NicholasM.: Sudden Stratospheric Warmings,
800 *Reviews of Geophysics*, 59, <https://doi.org/10.1029/2020rg000708>, 2021.
- 801 Bamston, A. G., Chelliah, M., and Goldenberg, S. B.: Documentation of a highly ENSO - related
802 sst region in the equatorial pacific: Research note, *Atmosphere-Ocean*, 35, 367 - 383,
803 <https://doi.org/10.1080/07055900.1997.9649597>, 1997.
- 804 Barriopedro, D. and Calvo, N.: On the Relationship between ENSO, Stratospheric Sudden
805 Warmings, and Blocking, *Journal of Climate*, 27, 4704–4720,
806 <https://doi.org/10.1175/jcli-d-13-00770.1>, 2014.
- 807 Butler, A. H. and Polvani, L. M.: El Niño, La Niña, and stratospheric sudden warmings: A
808 reevaluation in light of the observational record, *Geophysical Research Letters*, 38, n/a-n/a,
809 <https://doi.org/10.1029/2011gl048084>, 2011.
- 810 Domeisen, D. I. V., Garfinkel, C. I., and Butler, A. H.: The Teleconnection of El Niño Southern
811 Oscillation to the Stratosphere, *Reviews of Geophysics*, 57, 5–47,
812 <https://doi.org/10.1029/2018rg000596>, 2019.
- 813 Esler, J. G., Polvani, L. M., and Scott, R. K.: The Antarctic stratospheric sudden warming of 2002:
814 A self - tuned resonance?, *Geophysical Research Letters*, 33,
815 <https://doi.org/10.1029/2006gl026034>, 2006.
- 816 Evtushevsky, O. M., Kravchenko, V. O., Hood, L. L., and Milinevsky, G. P.: Teleconnection
817 between the central tropical Pacific and the Antarctic stratosphere: spatial patterns and time

- 818 lags, *Climate Dynamics*, 44, 1841–1855, <https://doi.org/10.1007/s00382-014-2375-2>, 2015.
- 819 Fogt, R. L., Bromwich, DavidH., and Hines, KeithM.: Understanding the SAM influence on the
820 South Pacific ENSO teleconnection, *Climate Dynamics*, 36, 1555–1576,
821 <https://doi.org/10.1007/s00382-010-0905-0>, 2011.
- 822 Garfinkel, C. I. and Hartmann, D. L.: Different ENSO teleconnections and their effects on the
823 stratospheric polar vortex, *Journal of Geophysical Research: Atmospheres*, 113,
824 <https://doi.org/10.1029/2008jd009920>, 2008.
- 825 Grassi, B., Redaelli, G., and Visconti, G.: Tropical SST Preconditioning of the SH Polar Vortex
826 during Winter 2002, *Journal of Climate*, 21, 5295–5303,
827 <https://doi.org/10.1175/2008jcli2136.1>, 2008.
- 828 Hersbach, H., Bell, B., Berrisford, P., Biavati, G., Horányi, A., Muñoz Sabater, J., Nicolas, J.,
829 Peubey, C., Radu, R., Rozum, I., Schepers, D., Simmons, A., Soci, C., Dee, D., and Thépaut,
830 J.-N.: ERA5 hourly data on pressure levels from 1940 to present, Copernicus Climate
831 Change Service (C3S) Climate Data Store (CDS), Dataset,
832 <https://doi.org/10.24381/cds.bd0915c6>, 2023a.
- 833 Hersbach, H., Bell, B., Berrisford, P., Biavati, G., Horányi, A., Muñoz Sabater, J., Nicolas, J.,
834 Peubey, C., Radu, R., Rozum, I., Schepers, D., Simmons, A., Soci, C., Dee, D., and Thépaut,
835 J.-N.: ERA5 hourly data on single levels from 1940 to present, Copernicus Climate Change
836 Service (C3S) Climate Data Store (CDS), Dataset, <https://doi.org/10.24381/cds.adbb2d47>,
837 2023b.
- 838 Honda, M., Inoue, J., and Yamane, S.: Influence of low Arctic sea-ice minima on anomalously
839 cold Eurasian winters. *Geophysical Research Letters*, 36(8).
840 <https://doi.org/10.1029/2008gl037079>, 2009.
- 841 Hoshi, K., Ukita, J., Honda, M., Iwamoto, K., Nakamura, T., Yamazaki, K., et al.: Poleward eddy
842 heat flux anomalies associated with recent Arctic sea ice loss. *Geophysical Research Letters*,
843 44(1), 446–454. <https://doi.org/10.1002/2016gl071893>, 2017.
- 844 Hu, Y. and Fu, Q.: Stratospheric warming in Southern Hemisphere high latitudes since 1979,
845 *Atmospheric Chemistry and Physics*, 9, 4329–4340,
846 <https://doi.org/10.5194/acp-9-4329-2009>, 2010.
- 847 Hu, Y., Tian, W., Zhang, J., Wang, T., and Xu, M.: Weakening of Antarctic stratospheric planetary
848 wave activities in early austral spring since the early 2000s: a response to sea surface
849 temperature trends, *Atmospheric Chemistry and Physics*, 22, 1575–1600,
850 <https://doi.org/10.5194/acp-22-1575-2022>, 2022.
- 851 Hurwitz, M. M., Newman, P. A., Oman, L. D., and Molod, A. M.: Response of the Antarctic
852 Stratosphere to Two Types of El Niño Events, *Journal of the Atmospheric Sciences*, 68,
853 812–822, <https://doi.org/10.1175/2011jas3606.1>, 2011a.
- 854 Hurwitz, M. M., Song, I.-S., Oman, L. D., Newman, P. A., Molod, A. M., Frith, S. M., and
855 Nielsen, J. E.: Response of the Antarctic stratosphere to warm pool El Niño Events in the
856 GEOS CCM, *Atmospheric Chemistry and Physics*, 11, 9659–9669,
857 <https://doi.org/10.5194/acp-11-9659-2011>, 2011b.

- 858 Ineson, S. and Scaife, A. A.: The role of the stratosphere in the European climate response to El
859 Niño, *Nature Geoscience*, 2, 32–36, <https://doi.org/10.1038/ngeo381>, 2009.
- 860 Karpetchko, A., Kyrö, E., and Knudsen, B. M.: Arctic and Antarctic polar vortices 1957 – 2002 as
861 seen from the ERA - 40 reanalyses, *Journal of Geophysical Research: Atmospheres*, 110,
862 <https://doi.org/10.1029/2005jd006113>, 2005.
- 863 Kim, B.-M., Choi, H., Kim, S.-J., and Choi, W.: Amplitude-dependent relationship between the
864 Southern Annular Mode and the El Niño Southern Oscillation in austral summer,
865 *Asia-Pacific Journal of Atmospheric Sciences*, 53, 85–100,
866 <https://doi.org/10.1007/s13143-017-0007-6>, 2017.
- 867 Kim, B.-M., Son, S.-W., Min, S.-K., Jeong, J.-H., Kim, S.-J., Zhang, X., et al.: Weakening of the
868 stratospheric polar vortex by Arctic sea-ice loss. *Nature Communications*, 5(1).
869 <https://doi.org/10.1038/ncomms5646>, 2014.
- 870 Kuroda, Y., Deushi, M., and Shibata, K.: Role of solar activity in the troposphere - stratosphere
871 coupling in the Southern Hemisphere winter, *Geophysical Research Letters*, 34,
872 <https://doi.org/10.1029/2007gl030983>, 2007.
- 873 L’Heureux, M. L. and Thompson, D. W. J.: Observed Relationships between the El
874 Niño–Southern Oscillation and the Extratropical Zonal-Mean Circulation, *Journal of*
875 *Climate*, 19, 276–287, <https://doi.org/10.1175/jcli3617.1>, 2006.
- 876 Laat, A. T. J., and Weele, M. V: The 2010 Antarctic ozone hole: Observed reduction in ozone
877 destruction by minor sudden stratospheric warmings, *Scientific Reports*, 1,
878 <https://doi.org/10.1038/srep00038>, 2011.
- 879 Lim, E., Hendon, H. H., and Thompson, D. W. J.: Seasonal Evolution of Stratosphere -
880 Troposphere Coupling in the Southern Hemisphere and Implications for the Predictability of
881 Surface Climate, *Journal of Geophysical Research: Atmospheres*, 123, 12,002-12,016,
882 <https://doi.org/10.1029/2018jd029321>, 2018.
- 883 Lim, E., Thompson, D., Butler, A., Wheeler, M., Nakamura, H., Jucker, M., Arblaster, J., Hendon.,
884 Newman, P., and Coy, L.: Characteristics of Antarctic Stratospheric Variability During
885 Winter: A Case Study of the 2024 Sudden Stratospheric Warming and Its Surface Impacts,
886 *Journal of Geophysical Research: Atmospheres*, 131, <https://doi.org/10.1029/2025jd045089>,
887 2026.
- 888 Lim, E., Zhou, L., Young, G., Abhik, S., Rudeva, I., Hope, P., Wheeler, M. C., Arblaster, J. M.,
889 Hendon, H. H., Manney, G., Son, S., Oh, J., and Garreaud, R. D.: Predictability of the 2020
890 Strong Vortex in the Antarctic Stratosphere and the Role of Ozone, *Journal of Geophysical*
891 *Research: Atmospheres*, 129, <https://doi.org/10.1029/2024jd040820>, 2024.
- 892 Lin, J. and Qian, T.: Impacts of the ENSO Lifecycle on Stratospheric Ozone and Temperature,
893 *Geophysical Research Letters*, 46, 10646–10658, <https://doi.org/10.1029/2019gl083697>,
894 2019.
- 895 Lin, P., Fu, Q., and Hartmann, D. L.: Impact of Tropical SST on Stratospheric Planetary Waves in
896 the Southern Hemisphere, *Journal of Climate*, 25, 5030–5046,
897 <https://doi.org/10.1175/jcli-d-11-00378.1>, 2012.

- 898 Lin, P., Fu, Q., Solomon, S., and Wallace, J. M.: Temperature Trend Patterns in Southern
899 Hemisphere High Latitudes: Novel Indicators of Stratospheric Change, *Journal of Climate*,
900 22, 6325–6341, <https://doi.org/10.1175/2009jcli2971.1>, 2009.
- 901 Ma, C., Yang, P., Tan, X., and Bao, M.: Possible Causes of the Occurrence of a Rare Antarctic
902 Sudden Stratospheric Warming in 2019, *Atmosphere*, 13, 147,
903 <https://doi.org/10.3390/atmos13010147>, 2022.
- 904 Manatsa, D. and Mukwada, G.: A connection from stratospheric ozone to El Niño-Southern
905 Oscillation, *Scientific Reports*, 7, <https://doi.org/10.1038/s41598-017-05111-8>, 2017.
- 906 Matsuno, T.: A Dynamical Model of the Stratospheric Sudden Warming. *Journal of the*
907 *Atmospheric Sciences*, 28(8), 1479–1494.
908 [https://doi.org/10.1175/1520-0469\(1971\)028<1479:admots>2.0.co;2](https://doi.org/10.1175/1520-0469(1971)028<1479:admots>2.0.co;2), 1971.
- 909 McPhaden, M. J., Zebiak, S. E., and Glantz, M. H.: ENSO as an Integrating Concept in Earth
910 Science, *Science*, 314, 1740–1745, <https://doi.org/10.1126/science.1132588>, 2006.
- 911 Mo, K.C. and Higgins, R. W.: The Pacific–South American Modes and Tropical Convection
912 during the Southern Hemisphere Winter, *Monthly Weather Review*, 126, 1581–1596,
913 [https://doi.org/10.1175/1520-0493\(1998\)126<1581:tpsama>2.0.co;2](https://doi.org/10.1175/1520-0493(1998)126<1581:tpsama>2.0.co;2), 1998.
- 914 Nakamura, H., Sampe, T., Goto, A., Ohfuchi, W., and Xie, S.: On the importance of midlatitude
915 oceanic frontal zones for the mean state and dominant variability in the tropospheric
916 circulation, *Geophysical Research Letters*, 35, <https://doi.org/10.1029/2008gl034010>, 2008.
- 917 Nakamura, T., Yamazaki, K., Iwamoto, K., Honda, M., Miyoshi, Y., Ogawa, Y., and Ukita, J.: A
918 negative phase shift of the winter AO/NAO due to the recent Arctic sea-ice reduction in late
919 autumn. *Journal of Geophysical Research: Atmospheres*, 3209–3227.
920 <https://doi.org/10.1002/2014jd022848>. 2015.
- 921 Niu, Y., Xie, F., and Wu, S.: ENSO Modoki Impacts on the Interannual Variations of Spring
922 Antarctic Stratospheric Ozone, *Journal of Climate*, 36, 5641–5658,
923 <https://doi.org/10.1175/jcli-d-22-0826.1>, 2023.
- 924 O'Neill, A., and C. Youngblut.: Stratospheric warmings diagnosed using the transformed
925 Eulerian-mean equations and the effect of the mean state on wave propagation. *Journal of*
926 *the Atmospheric Sciences*, 39, 1370 – 1386, doi:10.1175/1520-0469(1982)039,1370:
927 SWDUTT.2.0.CO;2. 1982.
- 928 Polvani, L. M., Sun, L., Butler, A. H., Richter, J. H., and Deser, C.: Distinguishing Stratospheric
929 Sudden Warmings from ENSO as Key Drivers of Wintertime Climate Variability over the
930 North Atlantic and Eurasia, *Journal of Climate*, 30, 1959–1969,
931 <https://doi.org/10.1175/jcli-d-16-0277.1>, 2017.
- 932 Rao, J., Garfinkel, C. I., Ren, R., Wu, T., and Lu, Y.: Southern Hemisphere Response to the
933 Quasi-Biennial Oscillation in the CMIP5/6 Models, *Journal of Climate*, 36, 2603–2623,
934 <https://doi.org/10.1175/jcli-d-22-0675.1>, 2023.
- 935 Rao, J., Garfinkel, C., White, I., and Schwartz, C.: The Southern Hemisphere Minor Sudden
936 Stratospheric Warming in September 2019 and its Predictions in S2S Models, *Journal of*
937 *Geophysical Research: Atmospheres*, 125, <https://doi.org/10.1029/2020jd032723>, 2020.

- 938 Rayner, N. A., Parker, D. E., Horton, E. B., Folland, C. K., Alexander, L. V., Rowell, D. P., Kent,
939 E. C., and Kaplan, A.: Global analyses of sea surface temperature, sea ice, and night marine
940 air temperature since the late nineteenth century, *Journal of Geophysical Research:*
941 *Atmospheres*, 108, <https://doi.org/10.1029/2002jd002670>, 2003.
- 942 Rea, D., Elsbury, D., Butler, A.H., Sun, L., Peings, Y., and Magnusdottir, G.: Interannual
943 Influence of Antarctic Sea Ice on Southern Hemisphere Stratosphere-Troposphere Coupling,
944 *Geophysical Research Letters*, 51, <https://doi.org/10.1029/2023gl1107478>, 2024.
- 945 Sampe, T., Nakamura, H., Goto, A., and Ohfuchi, W.: Significance of a Midlatitude SST Frontal
946 Zone in the Formation of a Storm Track and an Eddy-Driven Westerly Jet*, *Journal of*
947 *Climate*, 23, 1793 – 1814, <https://doi.org/10.1175/2009jcli3163.1>, 2010.
- 948 Shen, X., Wang, L., and Osprey, S.: Tropospheric Forcing of the 2019 Antarctic Sudden
949 Stratospheric Warming, *Geophysical Research Letters*, 47,
950 <https://doi.org/10.1029/2020gl089343>, 2020.
- 951 Silvestri, G. and Vera, C.: Nonstationary Impacts of the Southern Annular Mode on Southern
952 Hemisphere Climate, *Journal of Climate*, 22, 6142–6148,
953 <https://doi.org/10.1175/2009jcli3036.1>, 2009.
- 954 Singh, A. K. and Bhargawa, A.: Atmospheric burden of ozone depleting substances (ODSs) and
955 forecasting ozone layer recovery, *Atmospheric Pollution Research*, 10, 802–807,
956 <https://doi.org/10.1016/j.apr.2018.12.008>, 2019.
- 957 Solomon, S., Ivy, D. J., Kinnison, D., Mills, M. J., Neely, R. R., and Schmidt, A.: Emergence of
958 healing in the Antarctic ozone layer, *Science*, 353, 269–274,
959 <https://doi.org/10.1126/science.aae0061>, 2016.
- 960 Song, K. and Son, S.-W.: Revisiting the ENSO–SSW Relationship, *Journal of Climate*, 31,
961 2133–2143, <https://doi.org/10.1175/jcli-d-17-0078.1>, 2018.
- 962 Song, J., Zhang, J., Du, S., Xu, M., and Zhao, S.: Impact of Early Winter Antarctic Sea Ice
963 Reduction on Antarctic Stratospheric Polar Vortex, *Journal of Geophysical Research:*
964 *Atmospheres*, 130, <https://doi.org/10.1029/2024jd041831>, 2025.
- 965 Stone, K. A., Solomon, S., Thompson, D. W. J., Kinnison, D. E., and Fyfe, J. C.: On the Southern
966 Hemisphere stratospheric response to ENSO and its impacts on tropospheric circulation,
967 *Journal of Climate*, 35, 1963–1981, <https://doi.org/10.1175/jcli-d-21-0250.1>, 2022.
- 968 Sun, L., Deser, C., and Tomas, R.A.: Mechanisms of Stratospheric and Tropospheric Circulation
969 Response to Projected Arctic Sea Ice Loss, *Journal of Climate*, 28, 7824 – 7845,
970 <https://doi.org/10.1175/jcli-d-15-0169.1>, 2015.
- 971 Takaya, K. and Nakamura, H.: A Formulation of a Phase-Independent Wave-Activity Flux for
972 Stationary and Migratory Quasigeostrophic Eddies on a Zonally Varying Basic Flow, *Journal*
973 *of the Atmospheric Sciences*, 58, 608–627,
974 [https://doi.org/10.1175/1520-0469\(2001\)058<0608:afopi>2.0.co;2](https://doi.org/10.1175/1520-0469(2001)058<0608:afopi>2.0.co;2), 2001.
- 975 Thompson, D. W. J. and Solomon, S.: Interpretation of Recent Southern Hemisphere Climate
976 Change, *Science*, 296, 895–899, <https://doi.org/10.1126/science.1069270>, 2002.
- 977 Thompson, D. W. J., Baldwin, M. P., and Solomon, S.: Stratosphere–Troposphere Coupling in the

- 978 Southern Hemisphere, *Journal of the Atmospheric Sciences*, 62, 708–715,
979 <https://doi.org/10.1175/jas-3321.1>, 2005.
- 980 Thompson, D. W. J., Solomon, S., Kushner, P. J., England, M. H., Grise, K. M., and Karoly, D. J.:
981 Signatures of the Antarctic ozone hole in Southern Hemisphere surface climate change,
982 *Nature Geoscience*, 4, 741–749, <https://doi.org/10.1038/ngeo1296>, 2011.
- 983 Trenberth, K. E.: The Definition of El Niño, *Bulletin of the American Meteorological Society*, 78,
984 2771 – 2777, [https://doi.org/10.1175/1520-0477\(1997\)078<2771:tdoen>2.0.co;2](https://doi.org/10.1175/1520-0477(1997)078<2771:tdoen>2.0.co;2), 1997.
- 985 Wang, C.: A review of ENSO theories, *National Science Review*, 5, 813–825,
986 <https://doi.org/10.1093/nsr/nwy104>, 2018.
- 987 Wang, Z., Zhang, J., Zhao, S., and Li, D.: The joint effect of mid-latitude winds and the westerly
988 quasi-biennial oscillation phase on the Antarctic stratospheric polar vortex and ozone,
989 *Atmospheric Chemistry and Physics*, 25, 3465–3480,
990 <https://doi.org/10.5194/acp-25-3465-2025>, 2025.
- 991 Yang, C., Li, T., Dou, X., and Xue, X.: Signal of central Pacific El Niño in the Southern
992 Hemispheric stratosphere during austral spring, *Journal of Geophysical Research:
993 Atmospheres*, 120, <https://doi.org/10.1002/2015jd023486>, 2015.
- 994 Yang, X.-Y., Yuan, X., and Ting, M.: Dynamical Link between the Barents–Kara Sea Ice and the
995 Arctic Oscillation. *Journal of Climate*, 29(14), 5103–5122.
996 <https://doi.org/10.1175/jcli-d-15-0669.1>, 2016.
- 997 Zhang, R., Zhou, W., Tian, W., Zhang, Y., Liu, Z., and Cheung, P. K. Y.: Changes in the
998 Relationship between ENSO and the Winter Arctic Stratospheric Polar Vortex in Recent
999 Decades, *Journal of Climate*, 35, 5399–5414, <https://doi.org/10.1175/jcli-d-21-0924.1>, 2022.
- 1000 Zi, Y., Long, Z., Sheng, J., Lu, G., Perrie, W., and Xiao, Z.: The Sudden Stratospheric Warming
1001 Events in the Antarctic in 2024, *Geophysical Research Letters*, 52,
1002 <https://doi.org/10.1029/2025gl115257>, 2025.
- 1003 Zubiaurre, I. and Calvo, N.: The El Niño–Southern Oscillation (ENSO) Modoki signal in the
1004 stratosphere, *Journal of Geophysical Research: Atmospheres*, 117,
1005 <https://doi.org/10.1029/2011jd016690>, 2012.
- 1006